Chapter 8

Three-Dimensional Problems

In this chapter, we use the Method of Moments (MoM) to solve surface integral equation problems involving three-dimensional (3D) objects of arbitrary shape. This allows us to address many practical problems in areas such as electromagnetic interference (EMI), electronics packaging, scattering, radar cross section, and antenna design. The treatment of arbitrarily shaped 3D surfaces has received considerable attention in the literature, and many different methods have been proposed. We will consider one of the most commonly used approaches, where the surfaces are described using flat, planar triangles, and the currents expanded using the well-known Rao–Wilton–Glisson (RWG) basis functions. In Chapter 7, we treated several dielectric and dielectric/conducting junctions of limited type. In this chapter, we use the method outlined in [1] to treat junctions with much more general configurations.

Historically, the 3D problems that could be solved were limited to those of small electrical size, due to limitations in CPU time and system memory. Solving larger problems required access to supercomputer-class hardware, which was not available to most people. As computers have continued to become more powerful and less expensive over the last thirty or so years, much larger problems can now be solved on most desktop computers. This has also opened up areas of research that had never been attempted or considered before. For example, the development of matrix compression techniques, such as the Adaptive Cross Approximation (ACA), the Multi-Level Adaptive Cross Approximation (MLACA), and the Fast Multipole Method (FMM), has further increased the tractability of larger problems. These methods, discussed in the chapters that follow, will build on the material presented here.

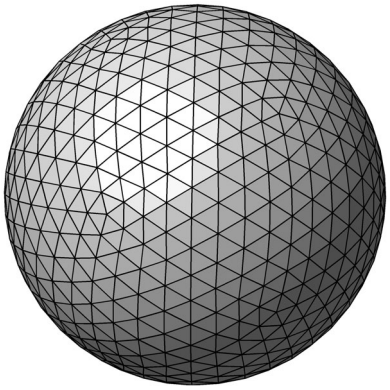
The approach in this chapter comprises four general steps: First, we consider the discretized EFIE, MFIE, and nMFIE of Section 3.6.2.2 in a region-wise context, and derive expressions for computing the required matrix elements. Next, we enforce the boundary conditions along each interface and at junctions, so that all linearly dependent unknowns are combined. We then reduce the resulting overdetermined matrix system by applying the integral equation formulations described in Section 3.6.3.1. Finally, we consider several numerical examples.

8.1 Modeling of Three-Dimensional Surfaces

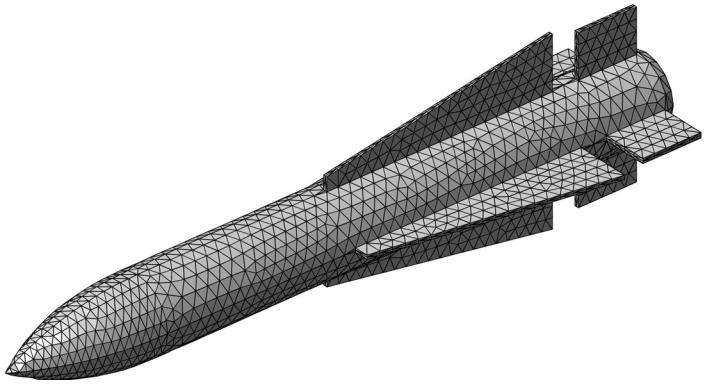
Let us consider the digital construction and representation of three-dimensional objects. First, a description of the object to be modeled is required. If the object is purely conceptual, line drawings or engineering blueprints are drafted, or if the actual object is available, drawings can be made via physical measurement. Next, a model of the object is constructed using a computer-aided design (CAD) program. This step often overlaps with the first, as the conceptual design and surface modeling of many objects can be done completely inside the CAD program, with no pen or paper required. The result is a digital, curved surface model that accurately represents the original geometry. Most modern modeling programs such as Rhinoceros 3D [2] represent free-form objects using a mathematically exact description such as non-uniform rational B-splines (NURBS) [3]. This approach preserves necessary information such as the surface normal and radius of curvature at every point. NURBS are used in many industry-standard CAD file formats and modeling engines, including IGES, STEP, ACIS, and Parasolid. Once the curved surface model is developed, it must then be reduced to a set of geometric primitives that can be processed. Among the most commonly used primitives are planar triangles (or *facets*), which are flexible and reasonably good at following the curvature of most realistic shapes [4]. Furthermore, numerical quadratures have been developed for the triangle (see Section 13.2), and analytic solutions to potential integrals exist for triangular subdomains [5, 6, 7, 8]. The model is then discretized, or *tessellated*, into a triangular mesh that conforms to the surfaces of interest, and most CAD programs can generate meshes of very high quality. Due to their flexibility, complex shapes such as ground and air vehicles can be represented with great precision by facet models. Figures 8.1a, 8.1b, and 8.1c depict a sphere, a missile, and a main battle tank represented entirely by triangular facets.

8.1.1 Facet File

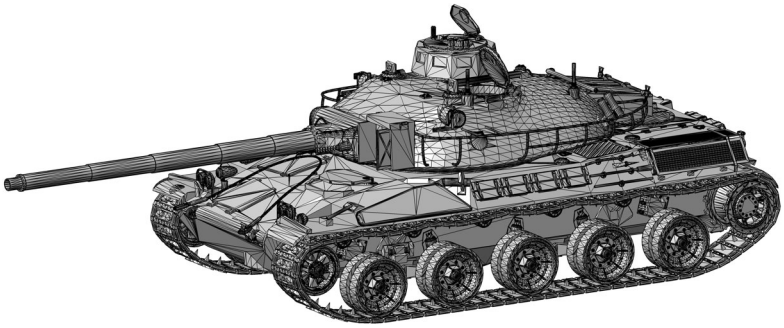
A common way to describe a triangular surface mesh is via the finite element connectivity file (or *facet file*) [9]. This file comprises a *node list* which contains the (x, y, z) components of all nodes in the mesh, and a *facet list* that comprises the indexes of the three nodes that define each triangle. Additional information regarding each triangle, such as its dielectric interface assignment, is often added to the facet list. An example is provided in Figure 8.2, which comprises a square plate in the xy plane constructed from 9 nodes and 8 triangles. In this example, a one-based indexing was used in the facet list.



(a) Sphere



(b) Missile



(c) Main Battle Tank

Figure 8.1: Example 3D Facet Models

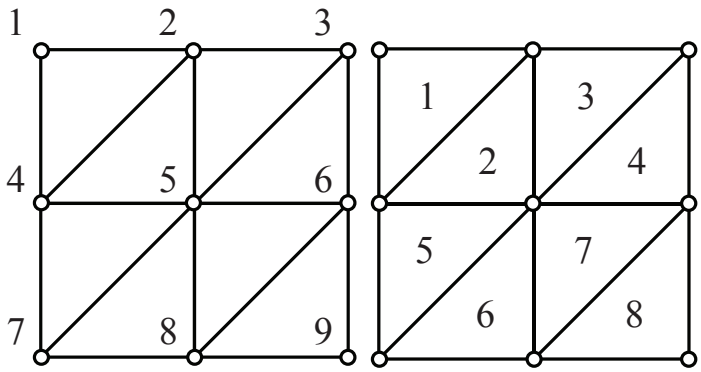
```
9
-1.0 1.0 0.0
 0.0 1.0 0.0
 1.0 1.0 0.0
-1.0 0.0 0.0
 0.0 0.0 0.0
 1.0 0.0 0.0
-1.0 -1.0 0.0
 0.0 -1.0 0.0
 1.0 -1.0 0.0
8
4 2 1
4 5 2
5 3 2
5 6 3
7 5 4
7 8 5
8 6 5
8 9 6
```

Figure 8.2: Example Facet File

8.1.2 Edge-Finding Algorithm

For a surface mesh, we need a way to identify and register all unique triangle edges. To illustrate the edge-finding algorithm, we use the facet file described in Figure 8.2. The numbering of the nodes and facets in this model is illustrated in Figures 8.3a and 8.3b, respectively. Our first task is to identify the connections between each node and each facet that references it. This will allow us to determine which facets share an edge. To do this, we create two lists for each node, a *node connectivity list* and a *facet connectivity list*. The first list contains all unique connections between each node and other nodes, and the second list contains the facets having that node as a vertex. We next loop over individual triangles and identify the nodes that make up the triangle, and sort them into ascending order. We then add the index of the current facet to the facet connectivity list of each node. For the node of lowest index, we add to its list the two higher node indexes if they are not already in the list. For the second node, the index of the third node is added to its list if not already present, and nothing is done for the third node. After this operation is completed, the node and facet connectivity lists are as shown in Table 8.1. Note that the node connectivity list contains no redundant links. This results in an empty list for node 9 since it is already referenced in the list for nodes 6 and 8.

At this point, the connectivity lists contain all the information needed to find the unique edges in the model. The remaining task is to go through the connectivity list for each node and create an edge for each entry. The facets common to the endpoints of each edge are recorded. If an edge belongs to only one triangle, it is called a *boundary*



(a) Node Numbering (b) Facet Numbering

Figure 8.3: Simple Flat Plate Geometry

Table 8.1: Node and Facet Connectivity Lists

Node #	Connected Nodes	Connected Facets
1	2 4	1
2	4 5 3	1 2 3
3	5 6	3 4
4	5 7	1 2 5
5	6 7 8	2 3 4 5 6 7
6	8 9	4 7 8
7	8	5 6
8	9	6 7 8
9	-	8

edge. Edges shared by two triangles are called *regular* edges (or just edges), and those shared by three or more facets are *junction* edges. Additional information regarding each edge can be stored at this step, such as its length, its endpoints, and which facets share it. Similarly, for each triangle we also store each of the unique edge indexes. This is useful for assigning basis function indexes later.

8.1.2.1 Shared Nodes

The edge-finding algorithm requires connected facets to use common node indices; otherwise, there is no logical connectivity, and the algorithm will not find any edges. Some CAD programs generate redundant nodes for each triangle, and some triangle file formats such as Stereolithography (.stl) store the nodes of each triangle separately. The CAD modeler should ensure that these redundant nodes are collapsed into single nodes. Some CAD programs have a function that will *join* or *weld* meshes to remove coincident nodes before finalizing the geometry, and some advanced MoM solver codes

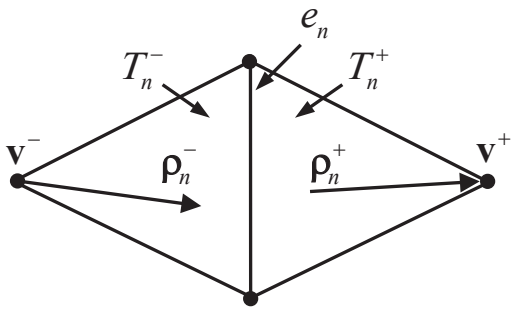


Figure 8.4: RWG Basis Function

will do this automatically when reading the facet file.

8.2 Expansion of Surface Currents

On each dielectric interface, the electric and magnetic currents are expanded as a sum of weighted basis functions as in (3.185) and (3.186). In the expansion, we use the Rao-Wilton-Glisson (RWG) basis function [10], which has become the most commonly used basis function in 3D problems since its introduction. The RWG function, as illustrated in Figure 8.4, is defined as

$$\mathbf{f}_n(\mathbf{r}) = \frac{L_n}{2A_n^+}\boldsymbol{\rho}_n^+(\mathbf{r}) \qquad \mathbf{r} \text{ in } T_n^+ \ , \tag{8.1}$$

$$\mathbf{f}_n(\mathbf{r}) = \frac{L_n}{2A_n^-}\boldsymbol{\rho}_n^-(\mathbf{r}) \qquad \mathbf{r} \text{ in } T_n^- \ , \tag{8.2}$$

$$\mathbf{f}_n(\mathbf{r}) = 0 \qquad \text{otherwise} \ , \tag{8.3}$$

where T_n^+ and T_n^- are a pair of triangles that share edge n, and L_n is the length of edge n. On T_n^+, the vector $\boldsymbol{\rho}_n^+(\mathbf{r})$ points *toward* the vertex $\mathbf{v}^+$ opposite the edge, and is

$$\boldsymbol{\rho}_n^+(\mathbf{r}) = \mathbf{v}^+ - \mathbf{r} \quad \mathbf{r} \text{ in } T_n^+ \ , \tag{8.4}$$

and on T_n^-, $\boldsymbol{\rho}_n^-(\mathbf{r})$ points *away* from the opposite vertex $\mathbf{v}^-$, and is

$$\boldsymbol{\rho}_n^-(\mathbf{r}) = \mathbf{r} - \mathbf{v}^- \quad \mathbf{r} \text{ in } T_n^- . \tag{8.5}$$

These basis functions are assigned only to *interior* edges shared by two or more adjacent triangles (we will discuss how RWG functions are assigned at junctions shortly). The RWG function has no component normal to any edge other than the one to which it is assigned, and its normal component at that edge is unity. Kirchhoff's current law is satisfied along each edge, and as boundary edges have no current flowing across them, they are not used. For Galerkin testing, we use the same RWG functions to test and expand the current.

The RWG functions comprise *first-order* or *linear* basis functions, however higher order basis functions on curvilinear (non-planar) triangles have also been studied, such as those in [11].

8.2.1 Divergence of the RWG Function

To compute the divergence of the RWG function, consider $\mathbf{f}_n(\mathbf{r})$ on T_n^-. If we now consider T_n^- in cylindrical coordinates, where $\mathbf{v}^-$ is the origin, $\mathbf{f}_n(\mathbf{r})$ can be written as a vector having only a radial component, yielding

$$\mathbf{f}_n(\mathbf{r}) = \frac{L_n}{2A_n^-} r\,\hat{\mathbf{r}}\,. \tag{8.6}$$

Taking the divergence in cylindrical coordinates then yields

$$\nabla \cdot \mathbf{f}_n(\mathbf{r}) = \frac{1}{r}\frac{\partial}{\partial r}\left[\frac{L_n}{2A_n^-} r^2\right] = \frac{L_n}{A_n^-} \quad \text{in } T_n^-, \tag{8.7}$$

and a similar calculation,

$$\nabla \cdot \mathbf{f}_n(\mathbf{r}) = -\frac{L_n}{A_n^+} \quad \text{in } T_n^+. \tag{8.8}$$

As the divergence of the current is proportional to the surface charge density through the equation of continuity, we see from (8.7) and (8.8) that the net charge associated with a pair of adjacent triangles is zero. As there is no accumulation of charges on an edge, the RWG function is said to be *divergence conforming* [11].

8.2.2 Assignment and Orientation of Basis Functions

Consider a problem of general configuration, comprising multiple dielectric and conducting regions, where there may be one or more junctions between regions. Let us now assign basis functions to the various interfaces on a region-wise basis. If e_n is a regular edge on the interface S_{lm} between dielectric regions R_l and R_m, we assign one electric and one magnetic basis function to the edge in each region. The functions are oriented so that they flow in opposite directions on each side of the interface, as illustrated in Figure 7.24a. If e_n is a junction edge, a similar assignment is made, except that the basis functions are oriented such that the current flows past the edge in a counterclockwise (or clockwise) direction, as shown in Figure 7.24b. These assignments ensure that Kirchhoff's current law is satisfied at e_n in each region. If the edge lies on a conducting interface or at a junction where one or more interfaces are conducting, we omit the magnetic basis function, as magnetic currents vanish on conductors. Similarly, no electric or magnetic basis functions are assigned inside a closed conducting region. Applying this procedure to all non-boundary edges leads to the discretized matrix system in (3.197), where the basis functions are oriented correctly but linear dependencies at the interfaces have not yet been taken into account. Section 8.6 discusses enforcement of the boundary conditions in detail.

8.3 EFIE

The EFIE (3.181) contains $\mathcal{L}$ and $\mathcal{K}$ operators, which were discretized and tested via the MoM in (3.188) and (3.189). In this section, we formulate expressions for both operators, using RWG basis and testing functions.

8.3.1 $\mathcal{L}$ Operator

Substitution of the electric basis and testing functions into (3.188) yields in Region R_l matrix elements given by

$$Z_{mn}^{EJ(l)} = \mathrm{L}(\mathbf{f}_m, \mathbf{f}_n) \,, \tag{8.9}$$

where

$$\mathrm{L}(\mathbf{f}_m, \mathbf{f}_n) = \int_{\mathbf{f}_m} \int_{\mathbf{f}_n} \left[j\omega\mu_l \, \mathbf{f}_m(\mathbf{r}) \cdot \mathbf{f}_n(\mathbf{r}') - \frac{j}{\omega\epsilon_l} \nabla \cdot \mathbf{f}_m(\mathbf{r}) \, \nabla' \cdot \mathbf{f}_n(\mathbf{r}') \right] \frac{e^{-jk_l r}}{4\pi r} \, d\mathbf{r}' \, d\mathbf{r} \,. \tag{8.10}$$

The inner and outer integrals in (8.10) are each performed over two triangles. However, as each triangle supports at most three basis and testing functions, the computations involving one source and testing triangle can contribute to as many as nine matrix elements. Thus, matrix filling will be most efficient by performing a loop over source and testing triangle pairs, where all possible combinations of basis and testing functions are considered for each pair.

8.3.1.1 Non-Near Terms

When the source and testing triangles are separated by a sufficient distance, (8.10) can be implemented as written. For a source and testing triangle, the contribution to (8.10) can be computed using an M-point numerical quadrature on each triangle, yielding

$$I = \frac{L_m L_n}{4\pi} \sum_{p=1}^{M} \sum_{q=1}^{M} w_p w_q \left[\frac{j\omega\mu_l}{4} \boldsymbol{\rho}_m^{\pm}(\mathbf{r}_p) \cdot \boldsymbol{\rho}_n^{\pm}(\mathbf{r}'_q) \pm \frac{j}{\omega\epsilon_l} \right] \frac{e^{-jk_l R_{pq}}}{R_{pq}} \,, \tag{8.11}$$

where p and q refer to the testing and source coordinates, respectively, and the quadrature weights w_p and w_q have been normalized with respect to triangle area. The distance R_{pq} is

$$R_{pq} = \sqrt{(x_p - x_q)^2 + (y_p - y_q)^2 + (z_p - z_q)^2} \,. \tag{8.12}$$

The signs of the terms in (8.11) depend on the orientations of the basis and testing functions on each triangle.

8.3.1.2 Near and Self Terms

When the source and testing triangles are close together or overlap, the integrations must be treated carefully. We use an approach similar to that used for the near and

self terms in Section 6.1.2, where the integral was rewritten as a sum of bounded and singular terms. We begin by rewriting the 3D Green's function in region R_l as

$$\frac{e^{-jk_l r}}{r} = \left[\frac{e^{-jk_l r}}{r} - \frac{1}{r}\right] + \frac{1}{r}\,, \tag{8.13}$$

which is often referred to in the literature as *singularity extraction*. The first term on the right-hand side is well behaved, and has the limit

$$\lim_{r\to 0}\left[\frac{e^{-jk_l r}}{r} - \frac{1}{r}\right] = -jk_l\,. \tag{8.14}$$

This portion can be used directly in (8.11). Substituting the second term on the right-hand side of (8.13) into (8.10) yields singular potential integrals of the form

$$I_1 = \int_T \int_{T'} \boldsymbol{\rho}_m^{\pm}(\mathbf{r}) \cdot \boldsymbol{\rho}_n^{\pm}(\mathbf{r}')\frac{1}{r}\, d\mathbf{r}'\, d\mathbf{r} \tag{8.15}$$

and

$$I_2 = \int_T \int_{T'} \frac{1}{r}\, d\mathbf{r}'\, d\mathbf{r}\,. \tag{8.16}$$

We will consider (8.15) and (8.16) separately for the self and near terms.

8.3.1.2.1 Self Terms

When T and T' overlap, the inner and outer integrals in (8.15) and (8.16) can be evaluated analytically. For brevity, we will consider the integrals in terms of the basis vectors $\boldsymbol{\rho}_{m,n}(\mathbf{r}) = \boldsymbol{\rho}_{m,n}^{-}(\mathbf{r})$ on T^-, and the corresponding results for $\boldsymbol{\rho}_{m,n}^{+}(\mathbf{r})$ can be obtained by a change of sign. To begin, we convert $\boldsymbol{\rho}_{m,n}(\mathbf{r})$ to simplex coordinates (see Section 13.2.1), yielding

$$\boldsymbol{\rho}_{m,n}(\mathbf{r}) = (1-\lambda_1-\lambda_2)\mathbf{v}_1 + \lambda_1\mathbf{v}_2 + \lambda_2\mathbf{v}_3 - \mathbf{v}_{m,n}\,, \tag{8.17}$$

where $\mathbf{v}_1, \mathbf{v}_2$ and $\mathbf{v}_3$ are the triangle nodes and $\mathbf{v}_{m,n}$ is the node opposite edge m or n on the triangle. Substitution of (8.17) into (8.15) yields

$$\begin{aligned} I_1 = \int_T \int_{T'} &\Big[(1-\lambda_1-\lambda_2)\mathbf{v}_1 + \lambda_1\mathbf{v}_2 + \lambda_2\mathbf{v}_3 - \mathbf{v}_m\Big] \\ &\cdot \Big[(1-\lambda_1'-\lambda_2')\mathbf{v}_1 + \lambda_1'\mathbf{v}_2 + \lambda_2'\mathbf{v}_3 - \mathbf{v}_n\Big]\frac{1}{r}\, d\lambda_1'\, d\lambda_2'\, d\lambda_1\, d\lambda_2\,. \end{aligned} \tag{8.18}$$

Expansion of all terms, and performing some lengthy term collection yields the integrand

$$\begin{aligned} \Big[&\lambda_1\lambda_1'(a_{11} - 2a_{12} + a_{22}) + \lambda_1\lambda_2'(a_{11} - a_{13} - a_{12} + a_{23}) \\ &+\lambda_2\lambda_2'(a_{11} - 2a_{13} + a_{33}) + \lambda_1'\lambda_2(a_{11} - a_{12} - a_{13} + a_{23}) \\ &+\lambda_1(-a_{11} + a_{1n} + a_{12} - a_{2n}) + \lambda_2(-a_{11} + a_{1n} + a_{13} - a_{3n}) \\ &+\lambda_1'(-a_{11} + a_{1m} + a_{12} - a_{2m}) + \lambda_2'(-a_{11} + a_{1m} + a_{13} - a_{3m}) \\ &+a_{11} - a_{1n} - a_{1m} + a_{mn}\Big]\frac{1}{r}\,, \end{aligned} \tag{8.19}$$

where

$$\begin{aligned}
a_{11} &= \mathbf{v}_1 \cdot \mathbf{v}_1, & a_{12} &= \mathbf{v}_1 \cdot \mathbf{v}_2, & a_{13} &= \mathbf{v}_1 \cdot \mathbf{v}_3, \\
a_{22} &= \mathbf{v}_2 \cdot \mathbf{v}_2, & a_{23} &= \mathbf{v}_2 \cdot \mathbf{v}_3, & a_{33} &= \mathbf{v}_3 \cdot \mathbf{v}_3, \\
a_{1n} &= \mathbf{v}_1 \cdot \mathbf{v}_n, & a_{1m} &= \mathbf{v}_1 \cdot \mathbf{v}_m, & a_{2n} &= \mathbf{v}_2 \cdot \mathbf{v}_n \\
a_{2m} &= \mathbf{v}_2 \cdot \mathbf{v}_m, & a_{3n} &= \mathbf{v}_3 \cdot \mathbf{v}_n, & a_{3m} &= \mathbf{v}_3 \cdot \mathbf{v}_m \\
& & a_{mn} &= \mathbf{v}_m \cdot \mathbf{v}_n \, . & & \qquad (8.20)
\end{aligned}$$

The result is a set of integrals of the form

$$\int_T \int_{T'} \lambda_i \lambda'_j \frac{1}{|\mathbf{r} - \mathbf{r}'|} \, dT \, dT', \qquad (8.21)$$

where the various permutations were evaluated analytically by Eibert and Hansen in [8, 12]. They are

$$\begin{aligned}
\frac{1}{4A^2} \int_T \int_{T'} \lambda_1 \lambda'_1 \frac{1}{|\mathbf{r} - \mathbf{r}'|} \, dT \, dT' &= \frac{\ln_1}{20 l_1} + \frac{l_1^2 + 5l_2^2 - l_3^2}{120 l_2^3} \ln_2 \\
&+ \frac{l_1^2 - l_2^2 + 5l_3^2}{120 l_3^3} \ln_3 + \frac{l_3 - l_1}{60 l_2^2} + \frac{l_2 - l_1}{60 l_3^2} \, , \qquad (8.22)
\end{aligned}$$

$$\begin{aligned}
\frac{1}{4A^2} \int_T \int_{T'} \lambda_1 \lambda'_2 \frac{1}{|\mathbf{r} - \mathbf{r}'|} \, dT \, dT' &= \frac{3l_1^2 + l_2^2 - l_3^2}{80 l_1^3} \ln_1 + \frac{l_1^2 + 3l_2^2 - l_3^2}{80 l_2^3} \ln_2 \\
&+ \frac{\ln_3}{40 l_3} + \frac{l_3 - l_2}{40 l_1^2} + \frac{l_3 - l_1}{40 l_2^2} \, , \qquad (8.23)
\end{aligned}$$

and

$$\begin{aligned}
\frac{1}{4A^2} \int_T \int_{T'} \lambda'_1 \frac{1}{|\mathbf{r} - \mathbf{r}'|} \, dT \, dT' &= \frac{\ln_1}{8 l_1} + \frac{l_1^2 + 5l_2^2 - l_3^2}{48 l_2^3} \ln_2 + \\
&\frac{l_1^2 - l_2^2 + 5l_3^2}{48 l_3^3} \ln_3 + \frac{l_3 - l_1}{24 l_2^2} + \frac{l_2 - l_1}{24 l_3^2} \, , \qquad (8.24)
\end{aligned}$$

where

$$l_1 = |\mathbf{v}_2 - \mathbf{v}_3| \, , \qquad (8.25)$$

$$l_2 = |\mathbf{v}_3 - \mathbf{v}_1| \, , \qquad (8.26)$$

$$l_3 = |\mathbf{v}_1 - \mathbf{v}_2| \, , \qquad (8.27)$$

and

$$\ln_1 = \log \frac{(l_1 + l_2)^2 - l_3^2}{l_2^2 - (l_3 - l_1)^2} \, , \qquad (8.28)$$

$$\ln_2 = \log \frac{(l_2 + l_3)^2 - l_1^2}{l_3^2 - (l_1 - l_2)^2} \, , \qquad (8.29)$$

$$\ln_3 = \log \frac{(l_3 + l_1)^2 - l_2^2}{l_1^2 - (l_2 - l_3)^2} \, . \qquad (8.30)$$

All integrals involving terms in the integrand of (8.19) can be obtained via (8.22–8.24) by permuting the vertex indices appropriately. The corresponding solution to (8.16) is

$$\frac{1}{4A^2}\int_T\int_{T'}\frac{1}{|\mathbf{r}-\mathbf{r}'|}\,dT\,dT' = \frac{\ln_1}{3l_1}+\frac{\ln_2}{3l_2}+\frac{\ln_3}{3l_3}. \tag{8.31}$$

Note that (8.31) does not depend on any basis function, so it need only be evaluated once per triangle.

8.3.1.2.2 Near Terms

When T and T' are close together, (8.15) and (8.16) must be treated carefully to achieve maximum accuracy. Following the approach used for the near terms in the thin wire EFIE, we evaluate the outer integral numerically and the inner integral analytically. For the inner integrals, we use the method outlined in [5], which gives analytic expressions for potential integrals over N sided planar polygons. As this method involves the triangle edges, consider the line segment C with endpoints $\mathbf{r}^-$ and $\mathbf{r}^+$ located in S (the plane of the polygon) as illustrated in Figure 8.5. The projections of source and observation vectors $\mathbf{r}'$ and $\mathbf{r}$ onto S are $\boldsymbol{\rho}'$ and $\boldsymbol{\rho}$, respectively. The quantities in the figure are computed as follows:

$$\boldsymbol{\rho}^\pm = \mathbf{r}^\pm - \hat{\mathbf{n}}(\hat{\mathbf{n}}\cdot\mathbf{r}^\pm)\,, \tag{8.32}$$

$$\hat{\mathbf{l}} = \frac{\boldsymbol{\rho}^+ - \boldsymbol{\rho}^-}{|\boldsymbol{\rho}^+ - \boldsymbol{\rho}^-|}\,, \tag{8.33}$$

$$\hat{\mathbf{u}} = \hat{\mathbf{l}}\times\hat{\mathbf{n}}\,, \tag{8.34}$$

$$l^\pm = (\boldsymbol{\rho}^\pm - \boldsymbol{\rho})\cdot\hat{\mathbf{l}}\,, \tag{8.35}$$

$$P^0 = |(\boldsymbol{\rho}^\pm - \boldsymbol{\rho})\cdot\hat{\mathbf{u}}|\,, \tag{8.36}$$

$$P^\pm = |(\boldsymbol{\rho}^\pm - \boldsymbol{\rho})| = \sqrt{(P^0)^2+(l^\pm)^2}\,, \tag{8.37}$$

$$\hat{\mathbf{P}}^0 = \frac{(\boldsymbol{\rho}^\pm - \boldsymbol{\rho}) - l^\pm\hat{\mathbf{l}}}{P^0}\,, \tag{8.38}$$

$$R^0 = \sqrt{(P^0)^2+d^2}\,, \tag{8.39}$$

and

$$R^\pm = \sqrt{(P^\pm)^2+d^2}. \tag{8.40}$$

The distance from the observation point to S is

$$d = \hat{\mathbf{n}}\cdot(\mathbf{r}-\mathbf{r}^\pm). \tag{8.41}$$

Using the above, integrals of the form

$$I_1 = \int_{T'}\frac{\boldsymbol{\rho}'-\boldsymbol{\rho}}{r}\,d\mathbf{r}' \tag{8.42}$$

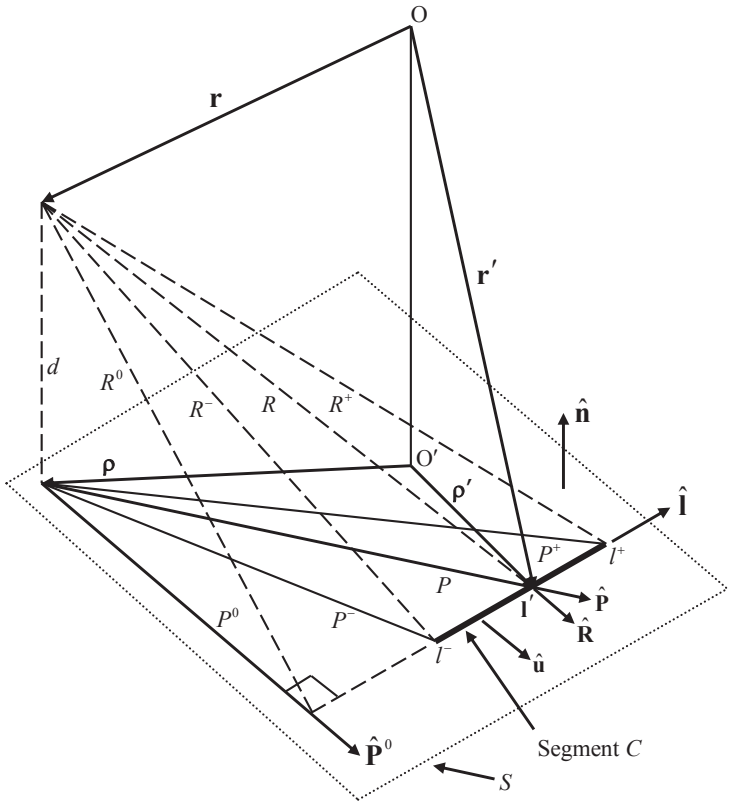


Figure 8.5: Geometric Quantities for Polygon Segment C

are evaluated via a sum over the N polygon edges given by

$$I_1 = \frac{1}{2}\sum_{i=1}^{N} \hat{\mathbf{u}}_i \left[(R_i^0)^2 \log \frac{R_i^+ + l_i^+}{R_i^- + l_i^-} + l_i^+ R_i^+ - l_i^- R_i^- \right]. \tag{8.43}$$

The integral

$$I_2 = \int_{T'} \frac{1}{r}\, d\mathbf{r}' \tag{8.44}$$

is evaluated similarly, yielding

$$I_2 = \sum_{i=1}^{N} \hat{\mathbf{P}}_i^0 \cdot \hat{\mathbf{u}}_i \left[P_i^0 \log \frac{R_i^+ + l_i^+}{R_i^- + l_i^-} - |d| \left(\tan^{-1} \frac{P_i^0 l_i^+}{(R_i^0)^2 + |d| R_i^+} - \tan^{-1} \frac{P_i^0 l_i^-}{(R_i^0)^2 + |d| R_i^-} \right) \right]. \tag{8.45}$$

Note that if the observation point $\boldsymbol{\rho}$ lies anywhere along an edge, the contribution from that edge to (8.43) is zero. Additionally, (8.43) and (8.45) suffer from numerical issues

when $\mathbf{r}$ lies in S along the extension of an edge ($R_i^0 = 0$). In such cases, the observation should be moved a very small distance away from the edge in the plane, i.e.,

$$\mathbf{r} = \mathbf{r} + \epsilon\hat{\mathbf{u}} \; . \tag{8.46}$$

To evaluate the innermost integral of (8.15), we write the basis function $\boldsymbol{\rho}_n(\mathbf{r}')$ as

$$\boldsymbol{\rho}_n(\mathbf{r}') = \boldsymbol{\rho}' - \boldsymbol{\rho}_n, \tag{8.47}$$

where $\boldsymbol{\rho}_n$ is the projection of $\mathbf{v}_n$ on S. We can then write

$$\boldsymbol{\rho}' - \boldsymbol{\rho}_n = (\boldsymbol{\rho}' - \boldsymbol{\rho}) + (\boldsymbol{\rho} - \boldsymbol{\rho}_n) \; , \tag{8.48}$$

which leads to

$$\int_{T'} \frac{\boldsymbol{\rho}_n(\mathbf{r}')}{r} \, d\mathbf{r}' = \int_{T'} \frac{\boldsymbol{\rho}' - \boldsymbol{\rho}}{r} \, d\mathbf{r}' + (\boldsymbol{\rho} - \boldsymbol{\rho}_n) \int_{T'} \frac{1}{r} \, d\mathbf{r}' \; . \tag{8.49}$$

The two integrals on the right can now be evaluated via (8.43) and (8.45), and the inner integral of (8.16) can be computed directly via (8.45). Integrals involving $\boldsymbol{\rho}_n^+(\mathbf{r})$ are obtained similarly, with a change of sign.

If both integrations were exact, interchanging the source and observation triangles in (8.15) and (8.16) would not change the result. Here, however, one integral is analytic and the other is numerical, so changing the order can produce slightly different results. To enforce symmetry, we perform a second integration with the triangles interchanged and average the results.

8.3.1.2.3 Duffy Transform

The Duffy transform [13, 14, 15, 16] is a method of regularizing integrals over a triangle with a $1/r$ singularity at a vertex, allowing a numerical quadrature to be used. The region of integration is converted from a triangle to a rectangle following the transformation

$$\int_T \frac{f(\mathbf{r}')}{r(\mathbf{r}')} \, d\mathbf{r}' = \int_0^1 \int_0^1 \frac{f(u,\gamma)}{r(u,\gamma)} |J(u,\gamma)| \, du \, d\gamma \; , \tag{8.50}$$

where $J(u,\gamma)$ is the Jacobian. To illustrate, let us apply the transform to the integral

$$\int_T \frac{1}{r} \, d\mathbf{r}' = \int_0^1 \int_0^1 \frac{|J(u,\gamma)|}{r(u,\gamma)} \, du \, d\gamma \; , \tag{8.51}$$

where the triangle is defined by the points $\mathbf{v}_1 = (x_1, y_1)$, $\mathbf{v}_2 = (x_2, y_2)$, and $\mathbf{v}_3 = (x_3, y_3)$, and the vector $\mathbf{r}'$ on T' is

$$\mathbf{r}' = (1-u)(1-\gamma)\mathbf{v}_1 + u\mathbf{v}_2 + \gamma(1-u)\mathbf{v}_3 \; . \tag{8.52}$$

The Jacobian is

$$\begin{aligned} J(u,\gamma) =& (1-u)\Big[\big(x_2 - x_1 + \gamma[x_1 - x_3]\big)\big(y_3 - y_1\big) \\ & - \big(y_2 - y_1 + \gamma[y_1 - y_3]\big)\big(x_3 - x_1\big)\Big], \end{aligned} \tag{8.53}$$

and fixing the observation (singular) point $\mathbf{r}$ at (x_1, y_1), r can be written as

$$r(x,y) = \sqrt{(x_1-x)^2 + (y_1-y)^2} = \sqrt{a(u,\gamma) + b(u,\gamma)} = r(u,\gamma)\ , \tag{8.54}$$

where

$$\begin{aligned} a(u,\gamma) = x_1^2 + ux_1x_2 + u^2x_2^2 + 2(1-u)(ux_2 - x_1)\Big[(1-\gamma)x_1 + \gamma x_3\Big] \\ +(1-u)^2\Big[(1-\gamma)x_1 + \gamma x_3\Big]^2, \end{aligned} \tag{8.55}$$

and

$$\begin{aligned} b(u,\gamma) = y_1^2 + uy_1y_2 + u^2y_2^2 + 2(1-u)(uy_2 - y_1)\Big[(1-\gamma)y_1 + \gamma y_3\Big] \\ +(1-u)^2\Big[(1-\gamma)y_1 + \gamma y_3\Big]^2. \end{aligned} \tag{8.56}$$

The resulting $(1-u)$ term in the numerator cancels the singularity in the denominator, allowing the integral to be evaluated using a numerical quadrature rule on a rectangular subdomain. When the observation point lies in the interior of the triangle, it can be divided into three sub-triangles with the new vertex placed at the singular point.

This method has several disadvantages. Because it remains purely numerical, its computational cost is relatively high because of the work required at each quadrature point. The transformation is also most accurate for triangles with reasonably good aspect ratios. Thinner triangles, on the other hand, require more quadrature points to retain the same level of accuracy [16]. Despite these drawbacks, the method remains attractive in cases where the function $f(\mathbf{r})$ is not integrable analytically.

8.3.1.2.4 Other Singularity Extractions

It was suggested in [16] that because the first term in (8.13) has a discontinuous derivative at $r = 0$, standard numerical quadrature may produce inaccurate results. They suggest the alternative singularity extraction given by

$$\frac{e^{-jkr}}{r} = \left[\frac{e^{-jkr}}{r} - \frac{1}{r} + \frac{k^2 r}{2}\right] + \frac{1}{r} - \frac{k^2 r}{2}\ , \tag{8.57}$$

where the first term has two continuous derivatives. The authors conclude that (8.57) is more accurate than (8.13) for the same number of quadrature points. In our experience, however, the extraction in (8.13) is sufficiently accurate for most three-dimensional problems. The appendix of [16] also gives expressions for evaluating integrals of the form

$$\int_T r^n\ d\mathbf{r}'\ , \tag{8.58}$$

$$\int_T r^n \left[\mathbf{r}' - \mathbf{v}\right]\ d\mathbf{r}'\ , \tag{8.59}$$

$$\int_T \nabla r^n\ d\mathbf{r}' \qquad \mathbf{r} \notin T\ , \tag{8.60}$$

and

$$\int_T \left[\nabla r^n\right]\left[\mathbf{r}' \times \mathbf{v}\right]\, d\mathbf{r}' \qquad \mathbf{r} \notin T\,, \tag{8.61}$$

where **v** is any vertex of T.

8.3.1.2.5 Example Singular Integral Evaluation

Let us compute (8.16) using (8.31) and (8.45). For the latter case, we apply a Gaussian quadrature rule of order N (Section 13.2.4) to compute the outermost integral. The integration domain is an equilateral triangle with sides of length 1. The results are summarized in Table 8.2. The comparison matches to two significant digits at higher quadrature orders, however the results demonstrate that for overlapping triangles (8.31) remains the superior choice. We next calculate (8.16) over a pair of co-planar equilateral triangles with sides of length 1, which share a common edge. For comparison, we will use Gaussian quadrature to compute both the inner and outer integrals, and then (8.45) to compute the innermost integral analytically, leaving the outer integration unchanged. The results are summarized in Table 8.3. The comparison is fairly good, suggesting that either method may be sufficient in this case. We now reduce the interior angle between the triangle faces to 10 degrees. The results are summarized in Table 8.4. The results from quadrature alone compare poorly to those using the analytic inner integration. It is clear from this example that analytic inner integration should be used to calculate all near matrix elements. To determine when to apply the near-integration formulas, the implementation can compare the distance between triangle centers. If that distance is less than a selected fraction of a wavelength, for example $\lambda/4$ or $\lambda/2$, the near-integration procedure is used.

Table 8.2: Overlapping Equilateral Triangle Double Integration

Order 1	Order 2	Order 3	Order 4	Order 5	Eqn. (8.31)
0.98767	0.85005	0.84709	0.83107	0.82830	0.82392

Table 8.3: Near Equilateral Triangle Double Integration (Co-planar)

Integration Method	Order 1	Order 2	Order 3	Order 4	Order 5
All Quadrature	0.32475	0.34364	0.34724	0.35330	0.35794
Quadrature + (8.45)	0.32922	0.34331	0.34553	0.34903	0.35009

Table 8.4: Near Equilateral Triangle Double Integration (Non Co-planar)

Integration Method	Order 1	Order 2	Order 3	Order 4	Order 5
All Quadrature	3.7357	2.1169	4.4860	1.5794	1.4878
Quadrature + (8.45)	0.86129	0.73681	0.73302	0.72283	0.72166

8.3.2 $\mathcal{K}$ Operator

Substitution of the magnetic basis and electric testing functions into (3.189) yields in Region R_l matrix elements given by

$$Z_{mn}^{EM(l)} = \mathrm{K}(\mathbf{f}_m, \mathbf{g}_n) \ , \tag{8.62}$$

where

$$\begin{aligned}\mathrm{K}(\mathbf{f}_m, \mathbf{g}_n) =& \frac{1}{2} \int_{\mathbf{f}_m, \mathbf{g}_n} \mathbf{f}_m(\mathbf{r}) \cdot \left[\hat{\mathbf{n}}_l(\mathbf{r}) \times \mathbf{g}_n(\mathbf{r})\right] \, d\mathbf{r} \\ & - \frac{1}{4\pi} \int_{\mathbf{f}_m} \mathbf{f}_m(\mathbf{r}) \cdot \int_{\mathbf{g}_n} \left[(\mathbf{r} - \mathbf{r}') \times \mathbf{g}_n(\mathbf{r}')\right] \frac{1 + jk_l r}{r^3} e^{-jk_l r} \, d\mathbf{r}' \, d\mathbf{r} \ . \end{aligned} \tag{8.63}$$

The first term on the right-hand side of (8.63) is used when the source and testing triangles overlap, and the second term is used when they do not.

8.3.2.1 Non-Near Terms

When the source and testing triangles are separated by a sufficient distance, (8.63) can be implemented as written. For a source and testing triangle, the contribution to (8.63) can be obtained using an M-point numerical quadrature, yielding

$$\eta_0 \frac{L_m L_n}{8A_m} \sum_{p=1}^{M} w_p \, \boldsymbol{\rho}_m^{\pm}(\mathbf{r}_p) \cdot \left[\hat{\mathbf{n}}_l(\mathbf{r}_p) \times \boldsymbol{\rho}_n^{\pm}(\mathbf{r}_p)\right] \tag{8.64}$$

when the triangles overlap, and

$$-\eta_0 \frac{L_m L_n}{16\pi} \sum_{p=1}^{M} \sum_{q=1}^{M} w_p w_q \, \boldsymbol{\rho}_m^{\pm}(\mathbf{r}_p) \cdot \left[(\mathbf{r}_p - \mathbf{r}_q') \times \boldsymbol{\rho}_n^{\pm}(\mathbf{r}_q')\right] \frac{1 + jk_l R_{pq}}{R_{pq}^3} e^{-jk_l R_{pq}} \tag{8.65}$$

when they do not. The quadrature weights are again normalized with respect to triangle area, and the variable signs depend on the orientation of the basis and testing functions on each triangle. The η_0 scale factor of the magnetic basis function has also been included in both terms.

8.3.2.2 Near Terms

When the source and testing triangles are closely spaced, the second term on the right-hand side of (8.63) exhibits strongly singular behavior, and special care must be taken when evaluating the integral. We use an approach similar to that used for the $\mathcal{L}$ operator. Following [17], we rewrite the inner integral, perform a singularity extraction, and evaluate the singular terms analytically. In addition to the quantities specified previously in Figure 8.5, we define the additional quantities shown in Figure 8.6, where $\boldsymbol{\rho}_n(\mathbf{r}') = \boldsymbol{\rho}_n^-(\mathbf{r}')$ on T_n^-.
Making the definition

$$\mathbf{R}_n = \mathbf{r} - \mathbf{v}_n \ , \tag{8.66}$$

where $\mathbf{v}_n$ is the vertex opposite edge n on T_n, and noting that

$$\mathbf{r} - \mathbf{r}' = \mathbf{R}_n - \boldsymbol{\rho}_n(\mathbf{r}') \,, \tag{8.67}$$

we can then write

$$(\mathbf{r} - \mathbf{r}') \times \boldsymbol{\rho}_n(\mathbf{r}') = \mathbf{R}_n \times \boldsymbol{\rho}_n(\mathbf{r}') \,. \tag{8.68}$$

Since $\mathbf{R}_n$ is a constant vector, the innermost integral in the second part of (8.63) can be written as

$$\int_{T_n} \Big[(\mathbf{r} - \mathbf{r}') \times \boldsymbol{\rho}_n(\mathbf{r}')\Big] \frac{1 + jk_l r}{r^3} e^{-jk_l r} \, d\mathbf{r}' = \mathbf{R}_n \times \int_{T_n} \boldsymbol{\rho}_n(\mathbf{r}') \frac{1 + jk_l r}{r^3} e^{-jk_l r} \, d\mathbf{r}' \,. \tag{8.69}$$

We next perform a singularity extraction following [17], resulting in

$$\mathbf{R}_n \times \int_{T_n} \boldsymbol{\rho}_n(\mathbf{r}') \frac{1 + jk_l r}{r^3} e^{-jk_l r} \, d\mathbf{r}' = \mathbf{R}_n \times \Bigg[\int_{T_n} \boldsymbol{\rho}_n(\mathbf{r}') \frac{(1 + jk_l r) e^{-jk_l r} - (1 + \frac{1}{2} k_l^2 r^2)}{r^3} \, d\mathbf{r}' + \mathbf{a}_n(\mathbf{r}) + \frac{k_l^2}{2} \mathbf{b}_n(\mathbf{r}) \Bigg], \tag{8.70}$$

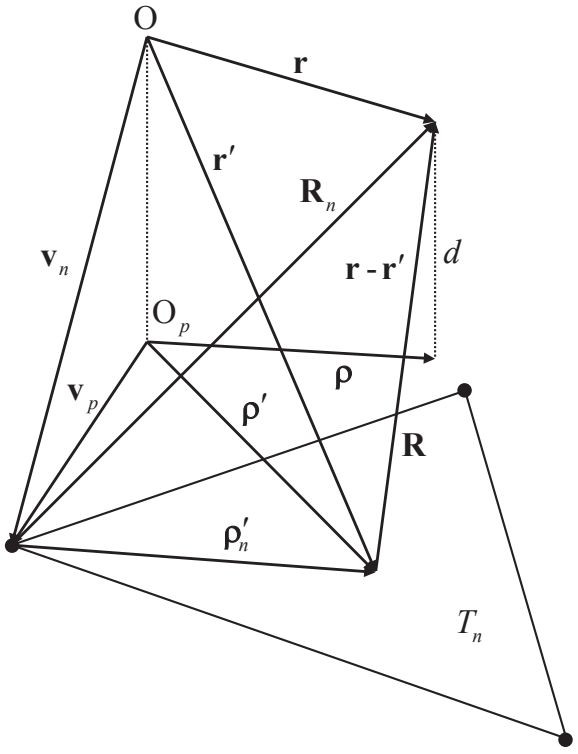


Figure 8.6: Geometric Quantities For $\mathcal{K}$ Operator Singularity Extraction

where

$$\mathbf{a}_n(\mathbf{r}) = \int_{T_n} \frac{\boldsymbol{\rho}_n(\mathbf{r}')}{r^3}\, d\mathbf{r}' \tag{8.71}$$

and

$$\mathbf{b}_n(\mathbf{r}) = \int_{T_n} \frac{\boldsymbol{\rho}_n(\mathbf{r}')}{r}\, d\mathbf{r}' \,. \tag{8.72}$$

The first term on the right-hand side in (8.70) is well behaved and can be evaluated using numerical quadrature. The remaining two integrals $\mathbf{a}_n(\mathbf{r})$ and $\mathbf{b}_n(\mathbf{r})$ are the singular contributions and will be evaluated analytically. The integral $\mathbf{b}_n(\mathbf{r})$ can be computed via (8.49). The integral $\mathbf{a}_n(\mathbf{r})$ can be computed by rewriting it following (8.48), which yields

$$\int_{T_n} \frac{\boldsymbol{\rho}_n(\mathbf{r}')}{r^3}\, d\mathbf{r}' = \int_{T_n} \frac{\boldsymbol{\rho}' - \boldsymbol{\rho}}{r^3}\, d\mathbf{r}' + (\boldsymbol{\rho} - \boldsymbol{\rho}_n) \int_{T_n} \frac{1}{r^3}\, d\mathbf{r}' \,. \tag{8.73}$$

The solutions to these integrals are [17]

$$\int_{T_n} \frac{\boldsymbol{\rho}' - \boldsymbol{\rho}}{r^3}\, d\mathbf{r}' = -\sum_{i=1}^{N} \hat{\mathbf{u}}_i \log \frac{R_i^+ + l_i^+}{R_i^- + l_i^-} \tag{8.74}$$

and

$$\begin{aligned} \int_{T_n} \frac{1}{r^3}\, d\mathbf{r}' = -\sum_{i=1}^{N} \hat{\mathbf{P}}_i^0 \cdot \hat{\mathbf{u}}_i \frac{1}{|d|} \Bigg[& \tan^{-1} \frac{|d| l_i^+}{P_i^0 R_i^+} - \tan^{-1} \frac{|d| l_i^-}{P_i^0 R_i^-} \\ & + \tan^{-1} \frac{l_i^-}{P_i^0} - \tan^{-1} \frac{l_i^+}{P_i^0} \Bigg] \end{aligned} \tag{8.75}$$

for $d \neq 0$, and

$$\int_{T_n} \frac{1}{r^3}\, d\mathbf{r}' = -\sum_{i=1}^{N} \hat{\mathbf{P}}_i^0 \cdot \hat{\mathbf{u}}_i \left[\frac{l_i^+}{P_i^0 R_i^+} - \frac{l_i^-}{P_i^0 R_i^-} \right] \tag{8.76}$$

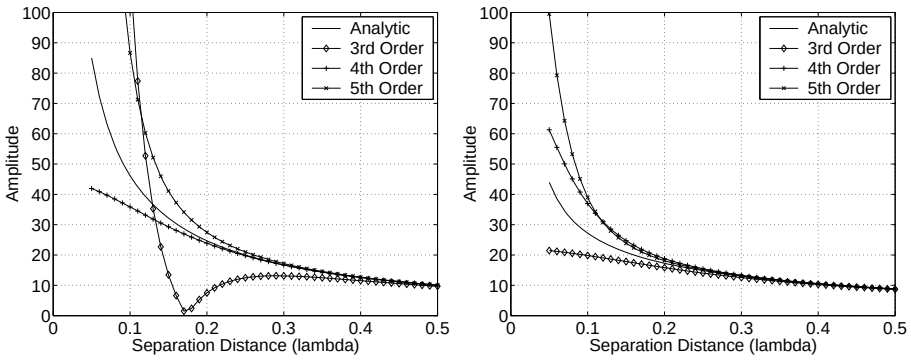
for $d = 0$. The sums in (8.74) and (8.76) may also have numerical problems when $\mathbf{r}$ lies in S along the extension of an edge. In these cases, the observation point can again be modified following (8.46). Results for $\boldsymbol{\rho}_n^+(\mathbf{r}')$ on T_n^+ are also obtained using (8.70) with a change of sign.

8.3.2.2.1 Example Singular Integral Evaluation

Let us compare Gaussian quadrature with the analytic solution (8.74–8.76) when computing the singular portion of (8.70). For this comparison, we compute the scalar quantity

$$\left| \mathbf{a}_n(\mathbf{r}) + \frac{k^2}{2} \mathbf{b}_n(\mathbf{r}) \right| . \tag{8.77}$$

The integrations are performed over an equilateral triangle with sides of length 1λ, and quadratures of order 3, 4, and 5. We first place the observation point above the center of



(a) Center of Triangle (b) Center of Edge

Figure 8.7: K Operator Near Integration

the triangle and vary the separation distance, with the results plotted in Figure 8.7a. The observation point is then placed above the midpoint of an edge, and the distance varied again, with results shown in Figure 8.7b. In both cases, the agreement is good at larger distances but degrades as the separation decreases, as expected. These results suggest that the singularity extraction method should be applied for triangle pairs separated by $\lambda/2$ or less.

8.3.3 Excitation

The right-hand side vector elements for the EFIE are given by (3.194). Using an M-point numerical quadrature, the contribution to (3.194) from a single testing triangle can be written as

$$\frac{L_m}{2}\sum_{p=1}^{M} w_p \boldsymbol{\rho}_m^{\pm}(\mathbf{r}_p)\cdot\mathbf{E}^i(\mathbf{r}_p)\;, \tag{8.78}$$

where the quadrature weights are normalized with respect to triangle area, and the variable sign depends on the orientation of the testing function on the triangle.

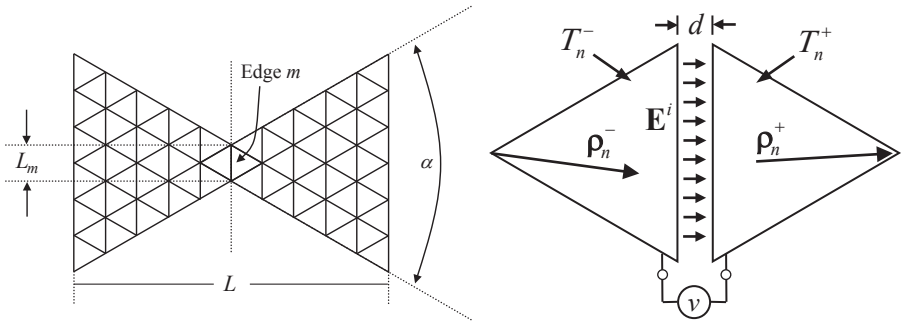
8.3.3.1 Plane Wave Excitation

For incident plane waves of $\hat{\boldsymbol{\theta}}^i$- or $\hat{\boldsymbol{\phi}}^i$-polarization having an electric field of unit amplitude, (3.194) in the exterior region R_0 can be written as

$$V_m^{E(\theta,\phi)} = \frac{L_m}{2A_m}(\hat{\boldsymbol{\theta}}^i,\hat{\boldsymbol{\phi}}^i)\cdot\int_{\mathbf{f}_m}\boldsymbol{\rho}_m^{\pm}(\mathbf{r})e^{jk_0\mathbf{r}\cdot\hat{\mathbf{r}}^i}\,d\mathbf{r}\;, \tag{8.79}$$

and following (8.78), the contribution from a single testing triangle is

$$\frac{L_m}{2}(\hat{\boldsymbol{\theta}}^i,\hat{\boldsymbol{\phi}}^i)\cdot\sum_{p=1}^{M} w_p\;\boldsymbol{\rho}_m^{\pm}(\mathbf{r}_p)e^{jk_0\mathbf{r}_p\cdot\hat{\mathbf{r}}^i}. \tag{8.80}$$



(a) Bowtie Antenna (b) Delta Gap at an Edge

Figure 8.8: Delta-Gap Feed Model

8.3.3.2 Planar Antenna Excitation

As planar antennas have many practical applications, they are often simulated during the design phase, which requires a model of the antenna feed terminals. In some applications, a high-fidelity feed model may be needed to obtain accurate results. Though such specialized models are beyond the scope of this text, the delta-gap model remains useful in computing impedance and radiation patterns in many cases. To develop a delta-gap model, consider the planar bowtie antenna illustrated in Figure 8.8a. We divide the antenna into two halves along edge m and connect a voltage generator of amplitude V_{in} to the triangles sharing the edge, as shown in Figure 8.8b. If we assume that a very small gap of width d exists between the two triangles, the electric field in the gap is

$$\mathbf{E}^i = \frac{V_{in}}{d}\hat{\mathbf{t}}_m \,, \tag{8.81}$$

where $\hat{\mathbf{t}}_m$ is the vector normal to edge m in the plane. Inserting (8.81) into (3.194), and using the fact that the normal component of the RWG function is unity along the edge, (3.194) evaluates to

$$V_m^{E(l)} = L_m V_{in} \,. \tag{8.82}$$

After solving the MoM linear system, the input impedance can be calculated. The electric current vector element $I_m^{J(l)}$ is the linear current density flowing across edge m. Therefore, the total electric current crossing the edge is

$$I_{in} = L_m I_m^{J(l)} \tag{8.83}$$

and the input impedance is

$$Z_{in} = \frac{V_{in}}{I_{in}} = \frac{V_{in}}{L_m I_m^{J(l)}} \,. \tag{8.84}$$

8.4 MFIE

The MFIE (3.182) also has $\mathcal{K}$ and $\mathcal{L}$ operators, which were discretized and tested via the MoM in (3.190) and (3.191). Substitution of the electric basis and magnetic testing functions into (3.190) yields in Region R_l matrix elements given by

$$Z_{mn}^{HJ(l)} = -\mathrm{K}(\mathbf{g}_m, \mathbf{f}_n) \,, \tag{8.85}$$

and substitution of the magnetic basis and testing functions into (3.191) yields

$$Z_{mn}^{HM(l)} = \frac{\epsilon_l}{\mu_l}\mathrm{L}(\mathbf{g}_m, \mathbf{g}_n) \,, \tag{8.86}$$

where the expressions for L and K were developed previously in Sections 8.3.1 and 8.3.2, respectively. Note that the L elements must be scaled by η_0^2 to account for the scale factors of the magnetic basis and testing functions.

8.4.1 Excitation

The right-hand side vector elements for the MFIE are given by (3.195). Using an M-point numerical quadrature, the contribution to (3.195) from a single testing triangle can be written as

$$\frac{L_m}{2}\sum_{p=1}^{M} w_p \boldsymbol{\rho}_m^{\pm}(\mathbf{r}_p)\cdot\mathbf{H}^i(\mathbf{r}_p) \,, \tag{8.87}$$

where the quadrature weights are normalized with respect to triangle area, and the variable sign depends on the orientation of the testing function on the triangle.

8.4.1.1 Plane Wave Excitation

Given $\hat{\boldsymbol{\theta}}^i$ and $\hat{\boldsymbol{\phi}}^i$-polarized incident electric fields, the corresponding magnetic fields are $-\hat{\boldsymbol{\phi}}^i$ and $\hat{\boldsymbol{\theta}}^i$-polarized, respectively. Thus, in the exterior region R_0 we can reuse the elements of the EFIE right-hand side, yielding MFIE right-hand side elements given by

$$V_m^{H,\theta} = -V_m^{E,\phi} \tag{8.88}$$

and

$$V_m^{H,\phi} = V_m^{E,\theta} \,. \tag{8.89}$$

8.5 nMFIE

The nMFIE (3.183) contains the $\hat{\mathbf{n}}\times\mathcal{L}$ and $\hat{\mathbf{n}}\times\mathcal{K}$ operators, which were discretized and tested via the MoM in (3.192) and (3.193). In this section, we formulate expressions for both operators, using RWG basis and testing functions.

8.5.1 $\hat{\mathbf{n}} \times \mathcal{K}$ Operator

Substituting the electric basis and testing functions into (3.192) yields in Region R_l matrix elements given by

$$Z_{mn}^{nHJ(l)} = \text{nK}(\mathbf{f}_m, \mathbf{f}_n) \ , \tag{8.90}$$

where

$$\text{nK}(\mathbf{f}_m, \mathbf{f}_n) = \frac{1}{2} \int_{\mathbf{f}_m, \mathbf{f}_n} \mathbf{f}_m(\mathbf{r}) \cdot \mathbf{f}_n(\mathbf{r}) \, d\mathbf{r}$$
$$+ \frac{1}{4\pi} \int_{\mathbf{f}_m} \mathbf{f}_m(\mathbf{r}) \cdot \left[\hat{\mathbf{n}}_l(\mathbf{r}) \times \int_{\mathbf{f}_n} \left[(\mathbf{r} - \mathbf{r}') \times \mathbf{f}_n(\mathbf{r}') \right] \frac{1 + jk_l r}{r^3} e^{-jk_l r} \, d\mathbf{r}' \right] d\mathbf{r} \ . \tag{8.91}$$

The first term on the right-hand side of (8.91) is used when the source and testing triangles overlap, and the second term is used when they do not. We note that (8.91) is almost identical to (8.63), except for the sign change on the second term and the relocation of $\hat{\mathbf{n}}_l(\mathbf{r})$.

8.5.1.1 Non-Near Terms

When the source and testing triangles are separated by a sufficient distance, (8.91) can be implemented as written. For a source and testing triangle, the contribution to (8.91) can be obtained using an M-point numerical quadrature, yielding

$$\frac{L_m L_n}{8A_m} \sum_{p=1}^{M} w_p \, \boldsymbol{\rho}_m^{\pm}(\mathbf{r}_p) \cdot \boldsymbol{\rho}_n^{\pm}(\mathbf{r}_p) \tag{8.92}$$

when the triangles overlap, and

$$\frac{L_m L_n}{16\pi} \sum_{p=1}^{M} \sum_{q=1}^{M} w_p w_q \, \boldsymbol{\rho}_m^{\pm}(\mathbf{r}_p) \cdot \left[\hat{\mathbf{n}}_l(\mathbf{r}_p) \times (\mathbf{r}_p - \mathbf{r}_q') \times \boldsymbol{\rho}_n^{\pm}(\mathbf{r}_q') \right] \frac{1 + jk_l R_{pq}}{R_{pq}^3} e^{-jk_l R_{pq}} \tag{8.93}$$

when they do not.

8.5.1.2 Near Terms

The innermost integral in the second part of (8.91) is identical to that of (8.63). Thus, the matrix-filling process can use this fact to compute the innermost integral of the K and nK terms simultaneously.

8.5.2 $\hat{\mathbf{n}} \times \mathcal{L}$ Operator

Substituting the magnetic basis and electric testing functions into (3.193) yields in Region R_l matrix elements given by

$$Z_{mn}^{nHM(l)} = \text{nL}(\mathbf{f}_m, \mathbf{g}_n) \ , \tag{8.94}$$

where

$$\mathrm{nL}(\mathbf{f}_m, \mathbf{g}_n) = j\omega\epsilon_l \int_{\mathbf{f}_m} \mathbf{f}_m(\mathbf{r}) \cdot \left[\hat{\mathbf{n}}_l(\mathbf{r}) \times \int_{\mathbf{g}_n} \mathbf{g}_n(\mathbf{r}') \frac{e^{-jk_l r}}{4\pi r}\, d\mathbf{r}'\right] d\mathbf{r}$$
$$-\frac{j}{\omega\mu_l} \oint_{\delta\mathbf{f}_m} \hat{\mathbf{c}}_m(\mathbf{r}) \cdot \left[\mathbf{f}_m(\mathbf{r}) \times \hat{\mathbf{n}}_l(\mathbf{r})\right] \int_{\mathbf{g}_n} \nabla' \cdot \mathbf{g}_n(\mathbf{r}') \frac{e^{-jk_l r}}{4\pi r}\, d\mathbf{r}'\, d\mathbf{r}\,, \qquad (8.95)$$

and (3.209) has been used to re-write the second part of (3.193). Note that since $\hat{\mathbf{c}}_m(\mathbf{r})$ is normal to the boundary in the plane of each triangle, it may have a different value along edge m in T_m^- than it does in T_m^+. Thus, the contour integral in the second part (8.5.2) must be performed over the boundaries of T_m^- and T_m^+ separately (a total of six edges).

8.5.2.1 Non-Near Terms

When the source and testing triangles are separated by a sufficient distance, (8.5.2) can be implemented as written. For a source and testing triangle, the contribution to (8.5.2) can be divided into two parts. The first term uses an M-point numerical quadrature over the source and testing triangles, given by

$$I_1 = j\omega\epsilon_l\eta_0 \frac{L_m L_n}{16\pi} \sum_{p=1}^{M}\sum_{q=1}^{M} w_p w_q \boldsymbol{\rho}_m^{\pm}(\mathbf{r}_p) \cdot \left[\hat{\mathbf{n}}_l(\mathbf{r}_p) \times \boldsymbol{\rho}_n^{\pm}(\mathbf{r}'_q)\right] \frac{e^{-jk_l R_{pq}}}{R_{pq}}\,. \qquad (8.96)$$

The second term uses a two-dimensional quadrature over the source triangle and a one-dimensional quadrature over the three edges of the testing triangle. This can be written as

$$I_2 = \pm\frac{j\eta_0}{\omega\mu_l} \frac{L_m L_n}{8\pi} \sum_{e=1}^{3}\sum_{p=1}^{M}\sum_{q=1}^{M} w_{e,p} w_q \mathbf{c}_m(\mathbf{r}_{e,p}) \cdot \left[\boldsymbol{\rho}_m^{\pm}(\mathbf{r}_{e,p}) \times \hat{\mathbf{n}}_l(\mathbf{r}_{e,p})\right] \frac{e^{-jk_l R_{pq}}}{R_{pq}}\,, \quad (8.97)$$

where the quadrature weights are again normalized, and the variable signs depend on the orientation of the basis and testing functions on each triangle. The η_0 scale factor of the magnetic basis function has also been included in both terms. Experience has shown that for a mesh having at least 10 edges per wavelength, 3 to 5 quadrature points per edge are sufficient for computing (8.97).

8.5.2.2 Near and Self Terms

For the near and self terms, we evaluate the inner integrals analytically and the outer integrals numerically. Because the inner integrals of both terms in (8.5.2) have the same form as (8.42) and (8.44), these expressions allow the L and nL near terms to be computed simultaneously.

8.5.3 Excitation

The right-hand side vector elements for the nMFIE are given by (3.196). Using an M-point numerical quadrature, the contribution to (3.196) from a single testing triangle

can be written as

$$\frac{L_m}{2}\sum_{p=1}^{M} w_p \boldsymbol{\rho}_m^{\pm}(\mathbf{r}_p)\cdot\Big[\hat{\mathbf{n}}_l(\mathbf{r}_p)\times\mathbf{H}^i(\mathbf{r}_p)\Big], \tag{8.98}$$

where the quadrature weights are normalized with respect to triangle area, and the variable sign depends on the orientation of the testing function on the triangle.

8.5.3.1 Plane Wave Excitation

Given $\hat{\boldsymbol{\theta}}^i$ and $\hat{\boldsymbol{\phi}}^i$-polarized incident electric fields, the corresponding magnetic fields are $-\hat{\boldsymbol{\phi}}^i$ and $\hat{\boldsymbol{\theta}}^i$-polarized, respectively. Thus, for an electric field of unit amplitude, the nMFIE right-hand side vectors in the exterior region R_0 can be written as

$$V_m^{nH(\theta,\phi)} = \frac{L_m}{2\eta_0 A_m}\int_{\mathbf{f}_m} \boldsymbol{\rho}_m^{\pm}(\mathbf{r})\cdot\Big[\hat{\mathbf{n}}_0(\mathbf{r})\times(-\hat{\boldsymbol{\phi}}^i,\hat{\boldsymbol{\theta}}^i)\Big]e^{jk_0\mathbf{r}\cdot\hat{\mathbf{r}}^i}\,d\mathbf{r}\,, \tag{8.99}$$

and following (8.98), the contribution to (8.99) from a single testing triangle is

$$\frac{L_m}{2\eta_0}\sum_{p=1}^{M} w_p\,\boldsymbol{\rho}_m^{\pm}(\mathbf{r}_p)\cdot\Big[\hat{\mathbf{n}}_0(\mathbf{r}_p)\times(-\hat{\boldsymbol{\phi}}^i,\hat{\boldsymbol{\theta}}^i)\Big]e^{jk_0\mathbf{r}_p\cdot\hat{\mathbf{r}}^i}. \tag{8.100}$$

8.6 Enforcement of Boundary Conditions

The matrix system (3.197) and basis functions have been defined region-wise, as discussed in Sections 3.6.3.1 and 8.2.2. The boundary conditions, however, stipulate linearly dependent unknowns that must be combined before the system can be solved. In this section, we present a generalized procedure for enforcing the boundary conditions along interfaces and junctions of general type, closely following the method outlined in [1].

8.6.1 Classification of Edges and Junctions

In treating the boundary conditions and imposing the desired integral equation formulation, we classify an edge e_n into one of three types:

1. **Dielectric edge or junction**: e_n lies on the intersection of two or more dielectric surfaces but does not touch any conducting surfaces.
2. **Conducting edge or junction**: e_n lies on the intersection of open or closed conducting surfaces but does not touch any dielectric surfaces.
3. **Composite conducting-dielectric junction**: e_n lies on the intersection of at least one open or closed conducting surface and at least one dielectric surface.

The following sections describe the rules for enforcing the boundary conditions at each type of edge or junction.

8.6.1.1 Dielectric Edges and Junctions

The boundary conditions along dielectric interfaces require the oriented basis functions assigned to regular edges or junctions to have the same coefficient. Therefore, following Section 7.10.1.1, all basis functions of the same type (electric or magnetic) assigned to e_n are combined. The first rule is therefore:

- **Rule 1**: Because the coefficients of the oriented basis functions of the same type assigned to a dielectric edge or junction have the same value, these unknowns must be combined into a single unknown. This is accomplished by combining the corresponding columns of the system matrix.

8.6.1.2 Conducting Edges and Junctions

We next consider the boundary conditions at conducting edges or junctions, which may contain a mixture of open and closed surfaces. Since the magnetic field is not necessarily continuous across a conducting surface, the electric current **J** must have independent values on the opposite sides of the surface. Thus, the electric basis functions assigned to a conducting edge or junction cannot be combined. There is, however, one exception to this rule: all conducting surfaces connected to e_n are open, and e_n lies entirely within a dielectric region. Consider an open conducting surface S lying completely inside a homogeneous dielectric region, where e_n comprises a regular edge on S that has been assigned the oriented electric basis functions $\mathbf{f}_1$ and $\mathbf{f}_2$. In a homogeneous region, these basis functions produce the same fields with opposite signs because of their orientations. Therefore, the fields can be generated by a single basis function, and one of the two functions can be removed. Generalizing this result to a junction of N conducting surfaces gives the second rule:

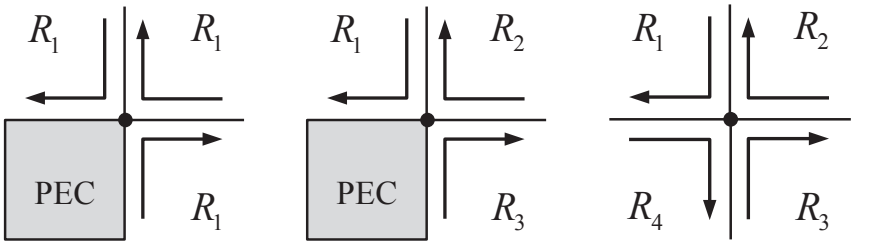
- **Rule 2**: As the magnetic field is not necessarily continuous across conducting surfaces, the electric basis functions assigned to a conducting edge or junction are independent. In addition, if all the surfaces meeting at e_n are open conducting surfaces, and e_n lies completely in the interior of a homogeneous dielectric region, one of the electric basis functions assigned to e_n is removed.

Several types of conducting edges and junctions that can be encountered are illustrated in Figures 8.9a–8.9e. In each figure, solid lines indicate open conducting surfaces, and the shaded areas are closed conducting regions. The basis functions drawn with dashed lines in Figures 8.9d and 8.9e indicate those that can be removed.

8.6.1.3 Composite Conducting-Dielectric Junctions

Now let e_n comprise a composite conducting-dielectric junction. Again, because the magnetic field is not continuous across open metallic surfaces, the electric current must have independent values on the opposite sides of any open conducting surface meeting at e_n. Combining this with the previously stated rules, we obtain our third rule:

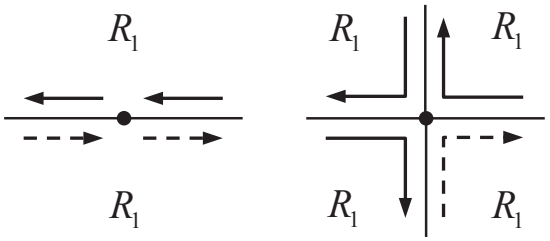
- **Rule 3**: Unknowns on opposite sides of open conducting surfaces meeting at a conducting-dielectric junction cannot be combined. In addition, unknowns on



(a) Junction of Closed and Open Surfaces in Single Region

(b) Junction of Closed and Open Surfaces in Multiple Regions

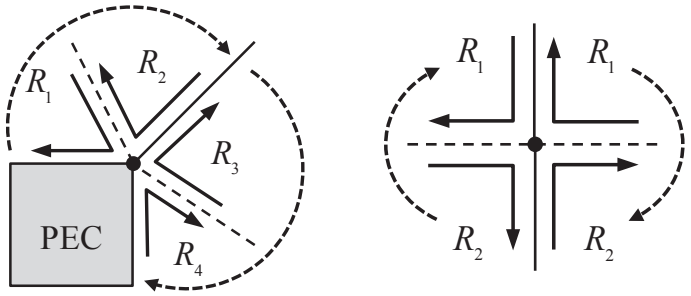
(c) Junction of Open Surfaces in Multiple Regions



(d) Conducting Edge on Open Surface in Single Region

(e) Conducting Junction between Open Surfaces in Single Region

Figure 8.9: Basis Functions at Conducting Edges and Junctions



(a) Closed and Open Conductors, Multiple Dielectric Regions

(b) Open Conductors, Two Dielectric Regions

Figure 8.10: Basis Functions at Composite Junctions

opposite sides of dielectric surfaces that lie in between open or closed conductors must be combined into a single unknown.

Two examples of composite junctions are illustrated in Figures 8.10a and 8.10b. Solid lines indicate open conducting surfaces, dashed lines indicate dielectric interfaces, and shaded areas are closed conducting regions. The curved, dashed arrows indicate where basis functions are combined.

8.6.2 Reducing the Overdetermined System

After the linearly dependent unknowns at edges and junctions have been combined by combining the corresponding columns of the system matrix, the resulting linear system is overdetermined. To obtain a well-defined system, the number of equations must be reduced to that of the remaining unknowns. The way this is done depends on the integral equation formulation. Our approach here is the EFIE-CFIE-PMCHWT approach of Section 3.6.3.1, where the EFIE and CFIE are applied at conducting edges and junctions, and PMCHWT is applied on dielectric edges and junctions. We will describe the approach in detail in this section.

8.6.2.1 PMCHWT at Dielectric Edges and Junctions

For a regular edge on the interface between two dielectric regions, the PMCHWT formulation is simply a summation of the EFIEs and MFIEs on each side of the interface. This can be generalized for dielectric junctions as follows. Let e_n be a dielectric edge or junction. We then sum the adjacent EFIEs and MFIEs, respectively, as

$$\sum_{l=1}^{M} \text{EFIE}_n^{(l)} \ , \tag{8.101}$$

and

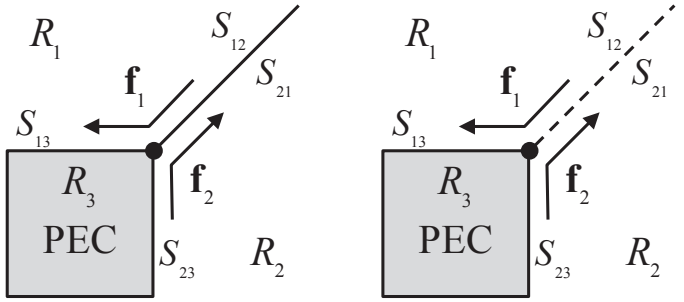
$$\sum_{l=1}^{M} \text{MFIE}_n^{(l)} \ , \tag{8.102}$$

where M is the number of dielectric regions meeting at e_n, and $\text{EFIE}_n^{(l)}$ and $\text{MFIE}_n^{(l)}$ comprise the EFIE and MFIE tested with the RWG function assigned to e_n in Region R_l. Doing this combines the corresponding rows of the system matrix.

8.6.2.2 EFIE and CFIE at Conducting Edges and Junctions

Let e_n be an edge on an open conducting surface, or a junction between several open conducting surfaces. If e_n is completely inside one dielectric region, by Rule 2 we have also removed one of the unknowns associated with the electric basis functions assigned to e_n. In addition, we now remove the EFIE from the system equations, which was tested with the corresponding electric basis function.

Next, let e_n be an edge on a closed conducting surface, or at the junction of a closed conducting surface and at least one open conducting surface. For each remaining electric basis function assigned to e_n, we combine the EFIE tested by the corresponding testing function on the open surfaces, with the CFIE (3.184) tested on the closed conducting surfaces.



(a) Conducting Junction with Open and Closed Conducting Surfaces

(b) Composite Junction with Closed Conducting Surface

Figure 8.11: Integral Equation Treatment at Junctions

For example, consider the junction in Figure 8.11a, where an open conducting surface (solid line) connects to a closed conducting region (shaded area). There are two dielectric regions R_1 and R_2 in addition to the closed conducting region R_3. As S_{12} (or S_{21}) is an open surface, the fields are not necessarily continuous across it, and following Rule 2, the electric basis functions $\mathbf{f}_1$ and $\mathbf{f}_2$ are considered to be independent. The choices of integral equations are as follows: The testing function associated with $\mathbf{f}_1$ will test in R_1 the EFIE on S_{12}, and the CFIE on S_{13}, which are added to a common matrix element. Likewise, the testing function associated with $\mathbf{f}_2$ will test in R_2 the EFIE on S_{21} and the CFIE on S_{23}.

8.6.2.3 EFIE and CFIE at Composite Conducting-Dielectric Junctions

Finally, we consider general conducting–dielectric junctions. If no closed conducting surfaces meet at e_n, then, by Rule 2, we combine the EFIEs between any two metallic surfaces using the sum

$$\sum_{l=1}^{M} \text{EFIE}_n^{(l)} \ , \tag{8.103}$$

where M is the number of dielectric regions between the surfaces. If a closed conducting surface meets at e_n, then the CFIEs are combined between any two metallic surfaces in a similar manner. To illustrate, consider the composite junction of Figure 8.11b, which is similar to that of 8.11a, except that S_{12} and S_{21} now comprise a dielectric interface. The choices of integral equations are as follows: The testing function associated with $\mathbf{f}_1$ will test in R_1 the CFIE on S_{12} and S_{13}. Likewise, the testing function associated with $\mathbf{f}_2$ will test in R_2 the CFIE on S_{21} and S_{23}. As the boundary conditions on S_{12} stipulate that $\mathbf{f}_1$ and $\mathbf{f}_2$ must have the same coefficient, the tested CFIEs that lie on and between S_{13} and S_{23} will contribute to the same matrix element.

8.7 Software Implementation Notes

In this section, we discuss practical aspects of implementing the techniques presented in this chapter in software, along with several important issues and considerations. Much of this material will be extended further in Chapters 9, 10, and 11.

8.7.1 Pre-Processing and Bookkeeping

In practice, the procedures outlined in Sections 8.2.2 and 8.6 reduce to a set of pre-processing steps that produce a bookkeeping database for constructing the system matrix. Because implementation details differ among software packages, we address these steps at a high level.

8.7.1.1 Region and Interface Assignments

The first step is to construct several lists. The first contains all unique dielectric regions and their material parameters ϵ and μ. Each region is assigned a unique ID, with free space and PEC assigned special values (such as 0 and -1) for internal use by the software. The second list describes all interfaces. Each interface is assigned a unique ID and the IDs of the regions on its interior and exterior sides, as determined by the surface normal. Each triangle is then assigned to an interface by appending the corresponding interface ID to each line of the connectivity list in the facet file. This is typically done when the facet file is constructed.

8.7.1.2 Geometry Processing

By applying the edge-finding algorithm (Section 8.1.2) to the facet file, we identify all boundary, regular, and junction edges in the triangle mesh, as well as the triangles (and interfaces) that connect to each edge. With the connectivity between neighboring triangles established, we can perform basic error checking. Triangles connected at a regular edge that are assigned to the incorrect interfaces can be found, and the presence of boundary (naked) edges on supposed closed interfaces can be reported to the user.

8.7.1.3 Assignment and Orientation of Basis Functions

Each triangle is now assigned two data structures: one stores the indices and orientations of the basis functions on the *interior* side of the triangle, and the other stores the corresponding data for the *exterior* side. These structures are populated by looping over all nonboundary edges and working in a local two-dimensional coordinate system. To illustrate, consider edge e_n with endpoints $\mathbf{e}_1$ and $\mathbf{e}_2$, which lies at the junction of M triangles. On triangle T_m, we denote the node opposite e_n as $\mathbf{v}_m$. We then define the reference axes in the local coordinate system as

$$\hat{\mathbf{z}} = \frac{\mathbf{e}_2 - \mathbf{e}_1}{|\mathbf{e}_2 - \mathbf{e}_1|}\,, \tag{8.104}$$

$$\hat{\mathbf{x}} = (\mathbf{v}_1 - \mathbf{e}_1) - \big[(\mathbf{v}_1 - \mathbf{e}_1)\cdot\hat{\mathbf{z}}\big]\hat{\mathbf{z}}\,, \tag{8.105}$$

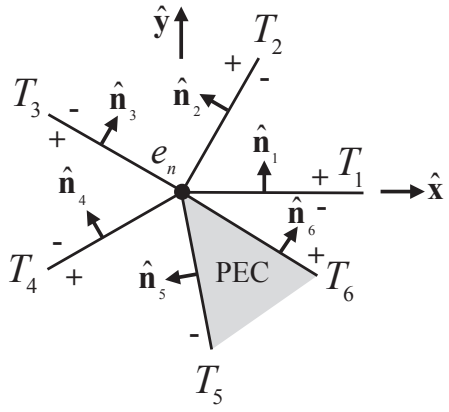


Figure 8.12: Local Reference Coordinates at Junction

and

$$\hat{\mathbf{y}} = \hat{\mathbf{z}} \times \hat{\mathbf{x}} \,, \tag{8.106}$$

where the plane of T_1 lies along the local $\hat{\mathbf{x}}$ axis. All other triangles at the junction are sorted counterclockwise, as shown in Figure 8.12. We then traverse the triangles in the counterclockwise direction. The normal vector of each triangle determines whether the data structure for its interior or exterior side is populated. The vector orientations of the basis functions at e_n are assigned in a back-to-front manner on each triangle, as indicated by the plus and minus signs. The rules in Section 8.6.1 are enforced at each step. The indices assigned to each basis function are obtained from running counts of the electric and magnetic basis functions already assigned. During the traversal of e_n, each count is either incremented or left unchanged, depending on the applicable rule. Once all edges have been processed, we add to each region a pointer to every triangle on its boundary and to the data structure assigned to the side of the triangle facing into the region.

8.7.2 Matrix and Right-Hand Side Fill

Matrix filling is performed on a per-region basis, as the integral operators depend on the wavenumber in each region. Inside a region, only those triangles and basis functions assigned to that region are considered. Similarly, right-hand side elements are computed only in regions where an impressed field exists. For scattering problems, this is the free space region R_0. The bookkeeping information generated during preprocessing determines the orientation and index of the basis and testing functions on the source and testing triangles, as well as the direction of the normal vector on each interface.

8.7.3 Parallelization

Many parts of an MoM solver can be parallelized effectively. The routines that compute the system matrix and right-hand side vectors are obvious candidates. Multiple right-hand sides can also be solved in parallel, as well as the matrix-vector product in an iterative solver. We now discuss several approaches for shared- and distributed-memory systems.

8.7.3.1 Shared Memory Systems

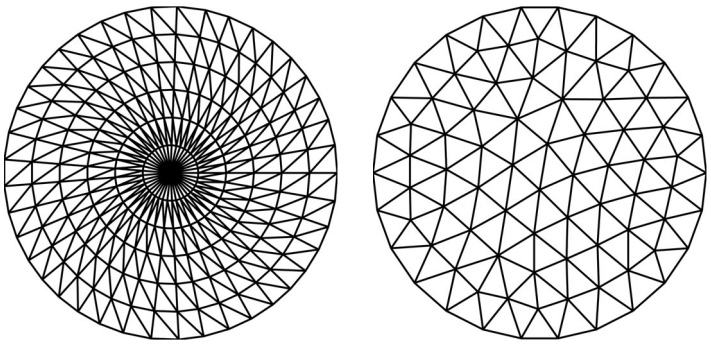
On a shared-memory system, all threads can address the geometry, bookkeeping information, and system matrix. Because system memory is almost always at a premium, a practical approach is to allocate a single system matrix and fill it in parallel. The matrix can be computed efficiently by looping over triangle pairs and evaluating the integral operators on separate threads. This approach requires synchronization whenever a value is added to the system matrix. Because the synchronization time is small relative to the operator-evaluation time, a simple mutex is generally sufficient to resolve thread contention. LAPACK routines are used for matrix factorization and right-hand-side solutions. Many implementations are single-threaded, although libraries such as the Intel Math Kernel Library (MKL) provide built-in parallelism. Because the storage required for the right-hand side vectors is small compared to the system matrix, multiple right-hand sides can be solved simultaneously in parallel. This is ideal for monostatic scattering problems, where the number of incidence angles may exceed the number of available processors. If the number of right-hand sides is small, individual right-hand side vectors can be computed by performing the required quadratures and assignments in parallel.

8.7.3.2 Distributed Memory Systems

The design and implementation of a solver on a distributed-memory system depend on several factors. The most important considerations are: the maximum size of the problem to be solved, the number and type of processors, the RAM available on each node, and the speed and topology of the network. In most cases, each node has enough memory to load and store the geometry and create the required bookkeeping data. It is the system matrix that is too large to be stored on a single node. In such a case, the matrix can be divided into blocks having roughly N/N_g rows and columns, where N is the total number of unknowns and N_g is the number of compute nodes. Each node is then responsible for computing and storing a subset of these blocks. After matrix filling is complete, a block LU factorization following Section 4.1.3 can be applied. For this, one option is to use the ScaLAPACK library [18], which implements a parallel, distributed memory LU factorization. A distributed algorithm designed specifically for an ACA-compressed block matrix is outlined in detail later in Section 9.6.3.2.

8.7.4 Triangle Mesh Considerations

The quality of the triangle mesh is one of the most important factors in any MoM simulation. Accurate integration of the matrix elements is essential, but the geometric



(a) Triangles with Poor Aspect Ratio (b) Triangles with Better Aspect Ratio

Figure 8.13: Examples of Triangle Mesh Aspect Ratio

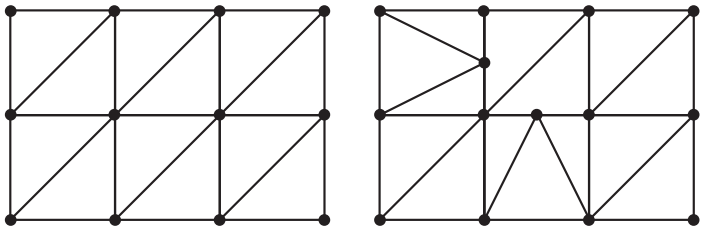
model itself is equally important. Generating a good model of a realistic object is not a trivial task, and considerable time and effort may be required to produce a triangular mesh that accurately describes the object and its dielectric interfaces and junctions. The model must also provide enough unknowns at the frequency of interest, be watertight, and be free of T-junctions and other errors.

8.7.4.1 Aspect Ratio

Most computer-aided design (CAD) tools can generate a triangular mesh from a curved surface, but mesh quality can vary. It is well known that meshes containing triangles with poor aspect ratios produce a more poorly conditioned system matrix. Thus, when building a mesh, care should be taken to ensure that each triangle has a reasonable aspect ratio and that it does not have small internal angles. An example of such a mesh is shown in Figure 8.13a, where we have meshed a circular plate using a very simple algorithm. The triangles in this mesh grow progressively smaller and thinner the closer they are to the center. Though it is not generally possible to create a mesh comprising perfectly equilateral triangles, many meshing tools will allow the user to analyze and adjust the distribution of aspect ratios in a mesh. In areas where the triangles are too thin, these tools often allow for restructuring or rebuilding the triangles to improve their shape. A better mesh is illustrated in Figure 8.13b, where the aspect ratios are improved.

8.7.4.2 T-Junctions

In Section 8.1.2.1 we discussed the importance of having shared nodes between triangles. If nodes are not joined at an edge, the surface will not have logical connectivity at the edge, and the edge-finding algorithm will not locate it. On interfaces that bound a closed region, the mesh must be free of any boundary or naked edges. Such a mesh is referred to as "watertight." Some CAD programs may generate meshes where the nodes of one triangle are not co-located with those of adjacent triangles. Consider the meshes shown in Figure 8.14. The mesh in Figure 8.14a is properly constructed, whereas the



(a) Properly Constructed Mesh (b) Mesh with T-Junctions

Figure 8.14: Triangle Mesh Connectivities

mesh in Figure 8.14b has several disconnected intersections called *T-junctions*. These connections cannot be logically resolved through the connectivity list, and will result in boundary edges where there should be none. When the number of triangles in the model grows to be quite high, T-junctions can become difficult to find and eliminate. Although it is sometimes necessary to remove T-junctions manually, most CAD programs can automatically locate and highlight these edges and, in some cases, repair the problem with little or no user intervention.

8.8 Numerical Examples

In this section, we use the methods developed in this chapter to compute the radar cross section of several test articles. We first consider conducting, dielectric, and coated spheres, followed by a set of benchmark targets constructed and measured by the Electromagnetic Code Consortium (EMCC) [19]. We then calculate the input impedance of several antennas, including the well-known bowtie and Archimedean spiral. Finally, we examine the monoconic reentry vehicle discussed in Section 7.10.2.4. The Rhinoceros 3D CAD software[1] was used to generate NURBS models of each object, which were then meshed using Altair HyperMesh. In each case, the meshes were generated with at least ten edges (unknowns) per wavelength in each dielectric region. PMCHWT was applied on dielectric interfaces, and the CFIE was applied on closed conductors with $\alpha = 0.5$.

8.8.1 Serenity

The examples in this chapter are computed using the Tripoint Industries code *Serenity*, part of the *lucernhammer* suite of radar cross section codes. Written in C++, *Serenity* implements the methods developed in this chapter, and supports multiple dielectric regions and junctions of general configuration. It includes an automatic edge-finding algorithm, adjustable Gaussian quadrature, and carefully implemented near- and self-term routines for all matrix elements.

[1] www.rhino3d.com

Serenity implements a full-matrix solver, as well as the compressed-matrix solvers discussed in the following chapters. The examples in this section were solved using the full-matrix solver, which is implemented on shared memory systems using POSIX threads (pthreads), with parallelized matrix filling, LU factorization, and right-hand side solution.

8.8.2 Compute Platform

Computations in this section were carried out on a Dell Precision T7910 workstation with two 12-core Intel Xeon E5-2690 v3 CPUs operating at 2.6 GHz and 256 GB of RAM, running Ubuntu Linux. *Serenity* was compiled using the GNU C++ Compiler (Version 7.5.0). The Intel Math Kernel Library (2019 version) was used for all BLAS and LAPACK functions. *Serenity* used 24 concurrent threads for matrix filling, LU factorization, and right-hand side solutions.

8.8.3 Spheres

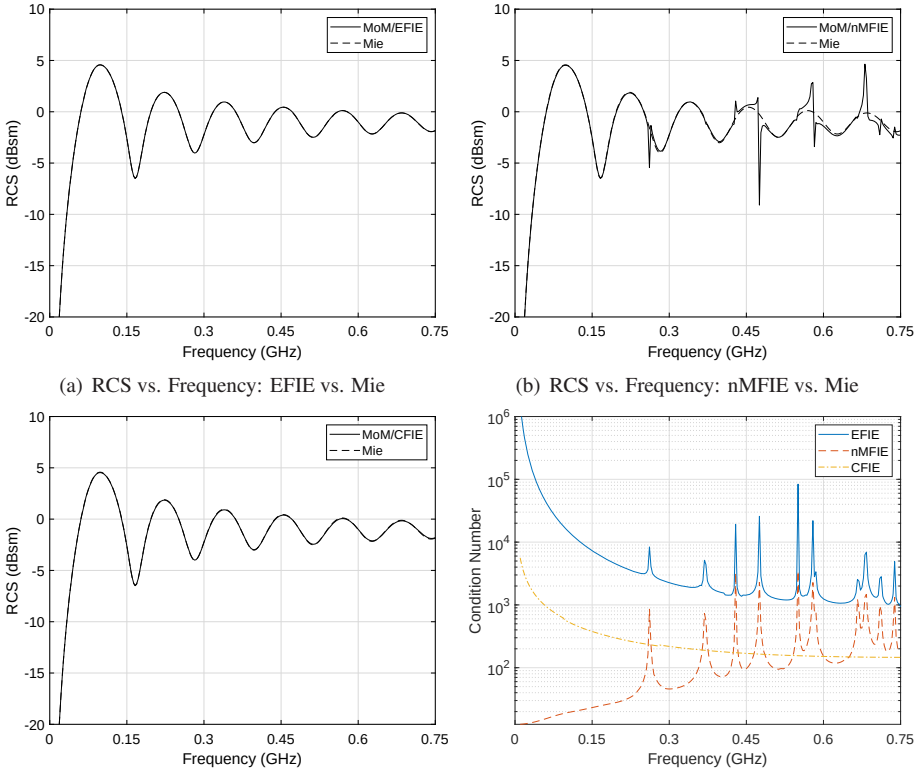
In this section, we compute the bistatic RCS of several conducting, fully dielectric, and coated spheres using the MoM, and compare the results to those obtained from the Mie series.

8.8.3.1 Conducting Sphere

In this section, we consider a conducting sphere with a radius of 0.5 meters. The analytic expressions for the scattered field of a conducting sphere were summarized previously in Section 7.9.1.1. For the MoM simulation, a facet model comprising 5120 near-equilateral triangles was constructed.

8.8.3.1.1 Monostatic RCS versus Frequency

We first compute the monostatic RCS for frequencies ranging from 10 to 750 MHz. In Figures 8.15a and 8.15b we compare the RCS obtained from the Mie series with that obtained from the MoM using the EFIE and nMFIE, respectively. The comparisons are good at lower frequencies, though as the frequency increases the nMFIE results become corrupted by internal resonances. Figure 8.15c shows the CFIE results, in which the resonance problems have been eliminated. Figure 8.15d shows the condition numbers obtained from the LAPACK function `cgecon` for each case. We note the periodic internal resonances in the EFIE and nMFIE results, which correspond with the corruptions seen in Figures 8.15a and 8.15b. The condition number for the CFIE remains smooth, as expected. We also note that the EFIE solution becomes singular at low frequencies, which is due to low-frequency breakdown of the discretized matrix elements resulting from the $\mathcal{L}$ operator. As $\omega \to 0$, the surface currents decouple into solenoidal (divergence-free) and irrotational (curl-free) components, and the contribution from the vector part of (8.10) becomes lost due to the frequency scaling [20]. This problem can be mitigated by using basis functions that model these components separately, such as the Loop-Star basis functions discussed in [21].



(a) RCS vs. Frequency: EFIE vs. Mie

(b) RCS vs. Frequency: nMFIE vs. Mie

(c) RCS vs. Frequency: CFIE vs. Mie

(d) Condition Number vs. Frequency

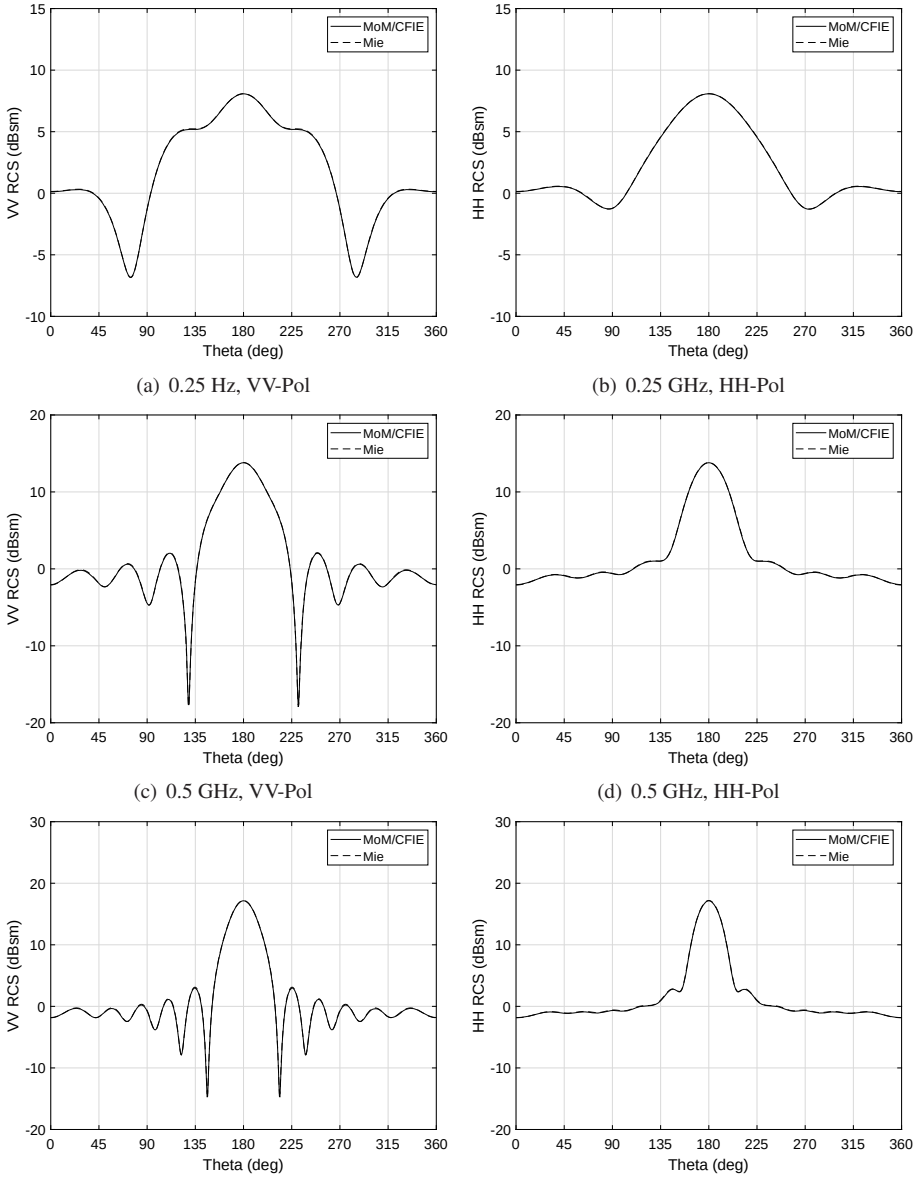
Figure 8.15: Conducting Sphere: RCS versus Frequency

8.8.3.1.2 Bistatic RCS

Using the same model and simulation parameters as before, we compute the bistatic RCS at 0.25, 0.5, and 0.75 GHz. The CFIE results are compared with those from the Mie series in Figures 8.16a–8.16f. The comparison is very good at all frequencies.

8.8.3.1.3 Near Field

Using (3.108), we next compute the near field of the conducting sphere illuminated by an $\hat{\mathbf{x}}$-polarized plane wave incident from the $+\hat{\mathbf{z}}$ direction at 750 MHz. In Figures 8.17a and 8.17b are shown the real part of the scattered and total electric field, respectively, in the yz plane.



(a) 0.25 Hz, VV-Pol

(b) 0.25 GHz, HH-Pol

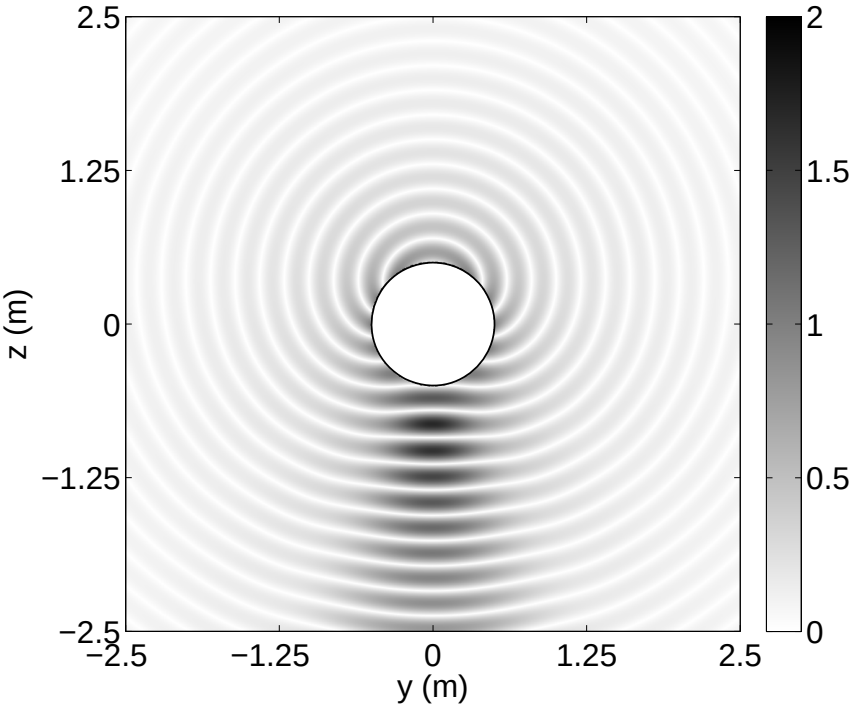
(c) 0.5 GHz, VV-Pol

(d) 0.5 GHz, HH-Pol

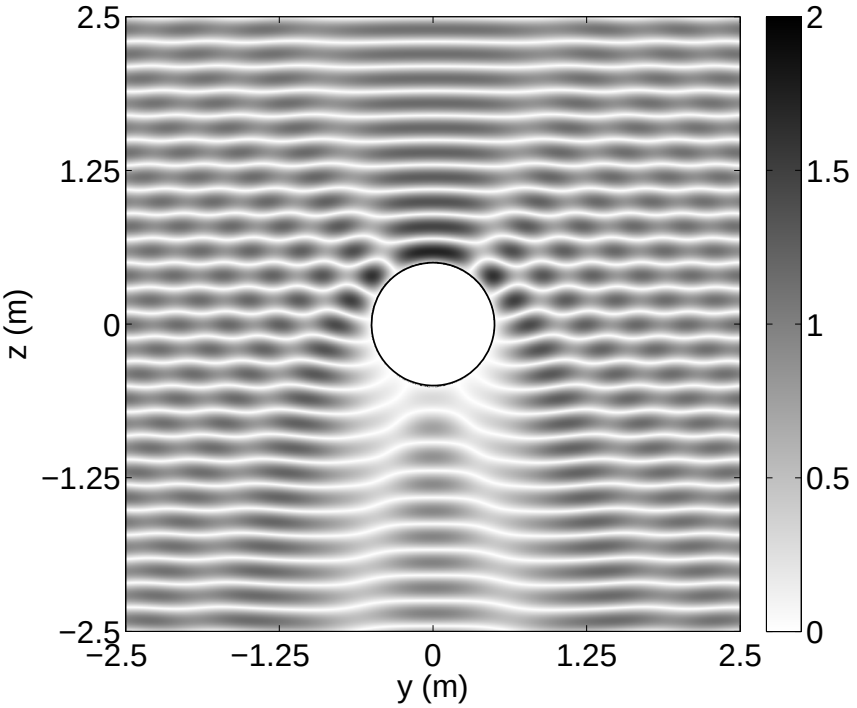
(e) 0.75 GHz, VV-Pol

(f) 0.75 GHz, HH-Pol

Figure 8.16: Conducting Sphere: Bistatic RCS



(a) Scattered Near Field ($|\mathrm{Re}(\mathbf{E}^s)|$, V/m)



(b) Total Near Field ($|\mathrm{Re}(\mathbf{E}^t)|$, V/m)

Figure 8.17: Conducting Sphere: Near Field at 750 MHz

8.8.3.2 Dielectric Sphere

In this section, we consider a dielectric sphere with a radius of 0.5 meters. The analytic expressions for the scattered field of a stratified sphere were summarized previously in Section 7.9.1.2. For the MoM simulation, we reuse the facet model from Section 8.8.3.1, and apply the PMCHWT formulation.

8.8.3.2.1 Monostatic RCS versus Frequency

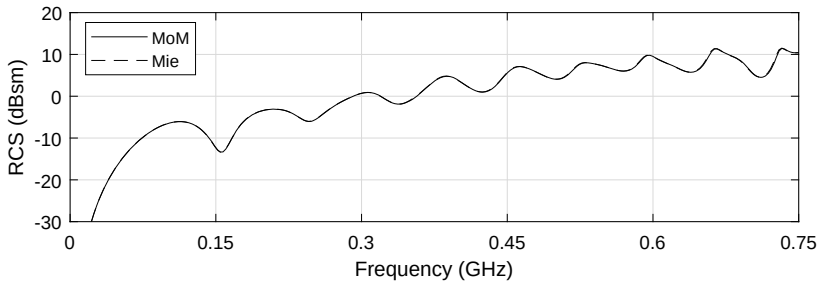
We first compute the RCS for frequencies ranging from 10 to 750 MHz. In Figure 8.18a we compare the RCS obtained by the Mie series to that of the MoM in backscattering ($\theta^i = \theta^s = 0$) for a lossless sphere ($\epsilon_r = 2.56$). The agreement is very good. In Figure 8.18b is a similar comparison for a lossy sphere ($\epsilon_r = 2.56 - j0.102$), where the agreement is again very good. The forward-scattering RCS ($\theta^i = 0, \theta^s = \pi$) for each case is summarized in Figures 8.19a and 8.19b, respectively, where the comparison is again quite good.

8.8.3.2.2 Bistatic RCS

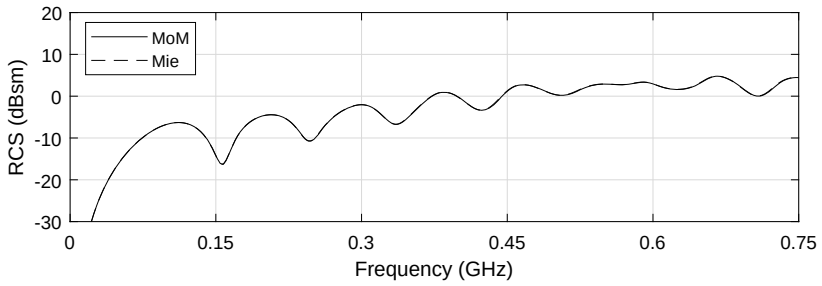
Using the same simulation parameters as before, we consider the bistatic RCS at 250, 500, and 750 MHz. The MoM results are compared with those of the Mie series for the lossless sphere in Figures 8.20a–8.20f. The comparison is very good. The results for the lossy sphere are compared in Figures 8.21a–8.21f, where the comparison is again very good.

8.8.3.2.3 Near Field

Using (3.108) and (3.112), we compute the near field of the lossless dielectric sphere illuminated by an $\hat{\mathbf{x}}$-polarized plane wave incident from the $+\hat{\mathbf{z}}$ direction at 750 MHz. Figures 8.22a and 8.22b show the real part of the scattered and total electric field, respectively, in the yz plane. To obtain the combined image, the total near fields are computed separately in the external and internal dielectric regions, and are then overlaid.

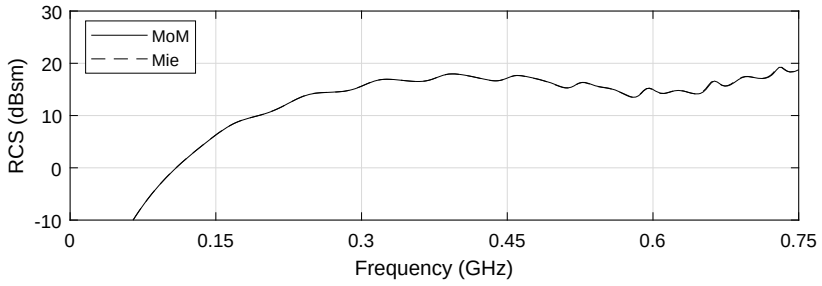


(a) Lossless Sphere ($\epsilon_r = 2.56$)

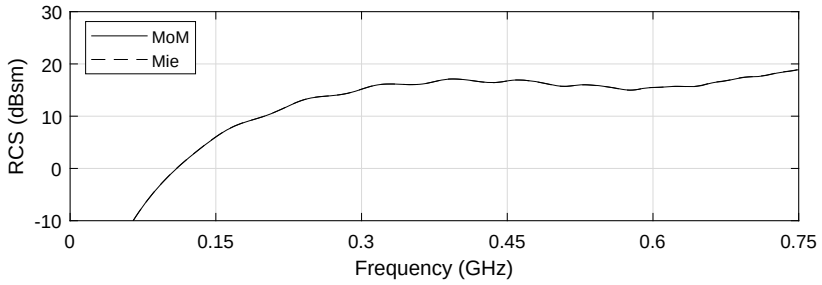


(b) Lossy Sphere ($\epsilon_r = 2.56 - j0.102$)

Figure 8.18: Dielectric Sphere: Backscatter RCS vs. Frequency

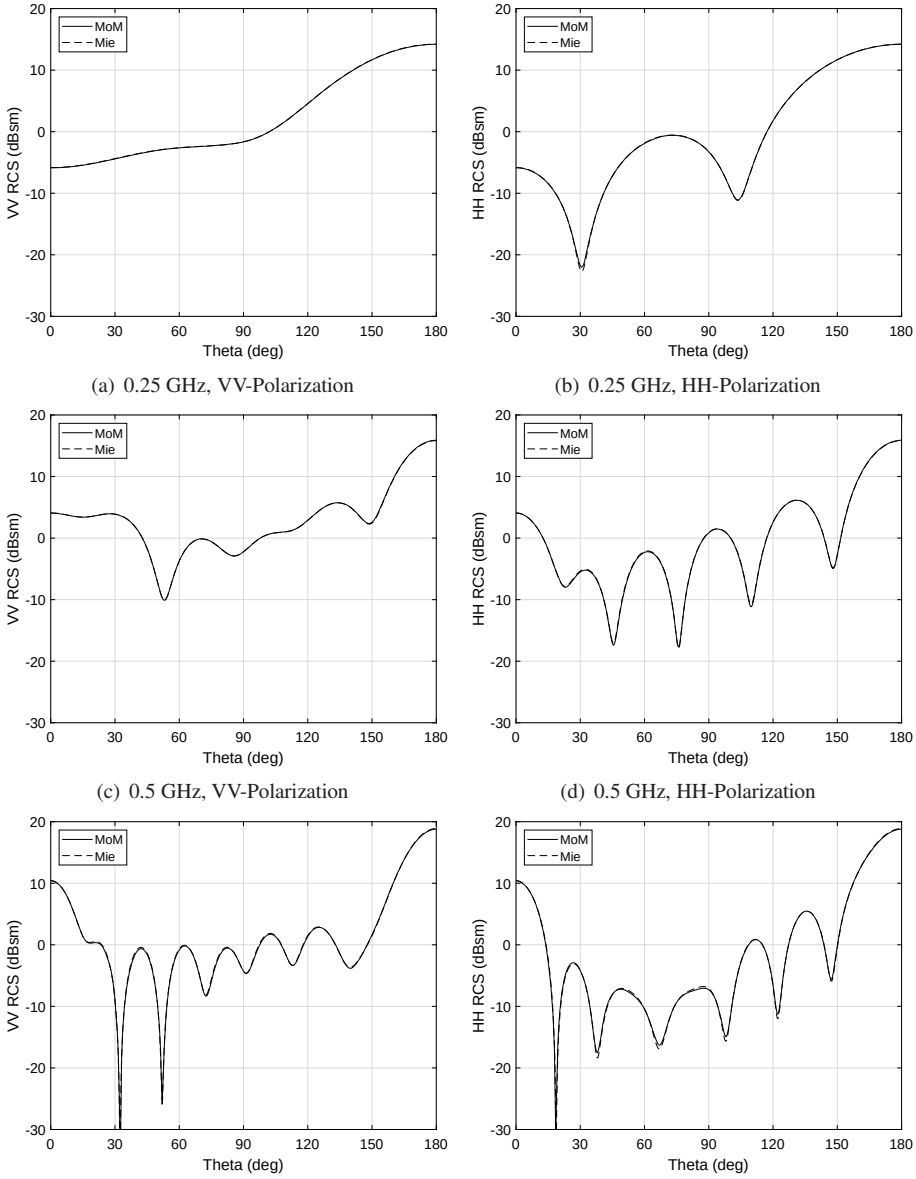


(a) Lossless Sphere ($\epsilon_r = 2.56$)



(b) Lossy Sphere ($\epsilon_r = 2.56 - j0.102$)

Figure 8.19: Dielectric Sphere: Forward Scatter RCS vs. Frequency



(a) 0.25 GHz, VV-Polarization

(b) 0.25 GHz, HH-Polarization

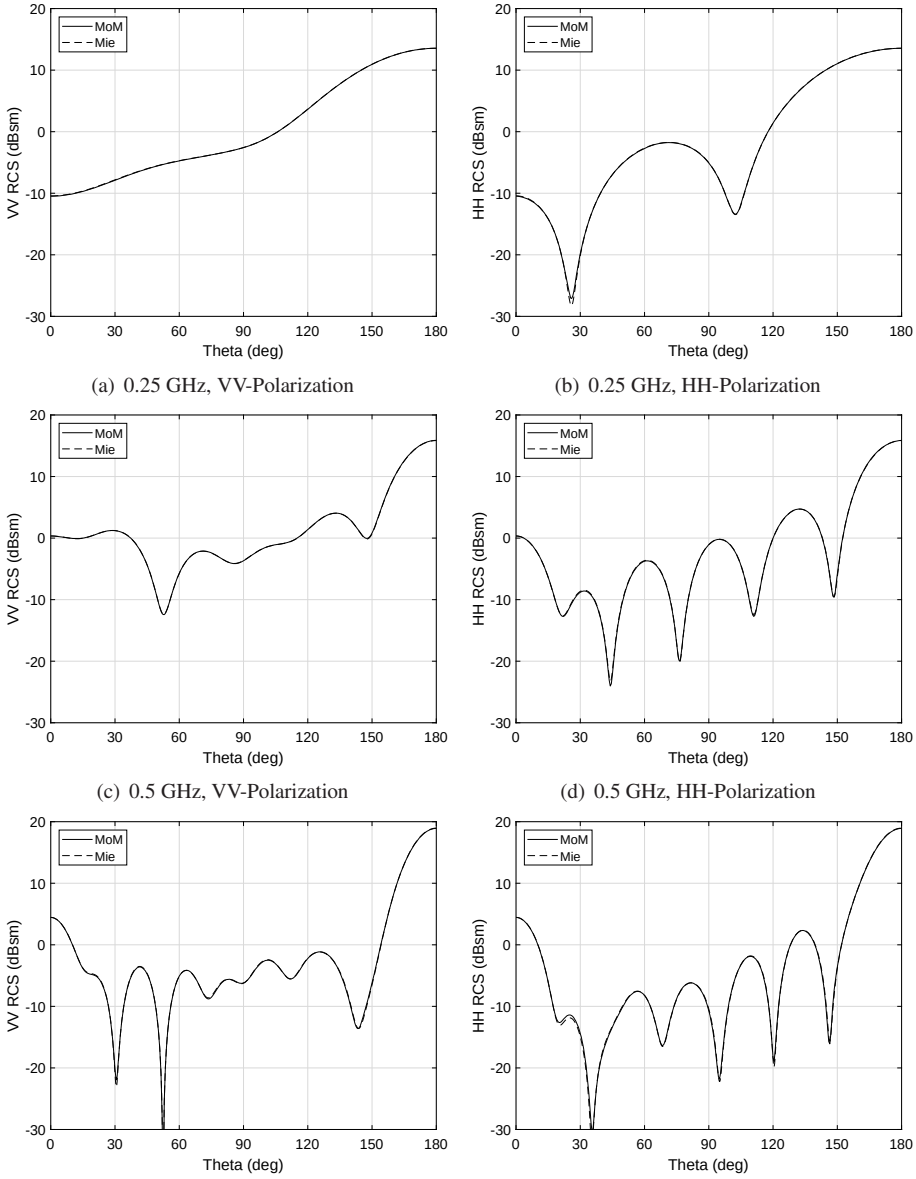
(c) 0.5 GHz, VV-Polarization

(d) 0.5 GHz, HH-Polarization

(e) 0.75 GHz, VV-Polarization

(f) 0.75 GHz, HH-Polarization

Figure 8.20: Lossless Dielectric Sphere ($\epsilon_r = 2.56$): Bistatic RCS



(a) 0.25 GHz, VV-Polarization

(b) 0.25 GHz, HH-Polarization

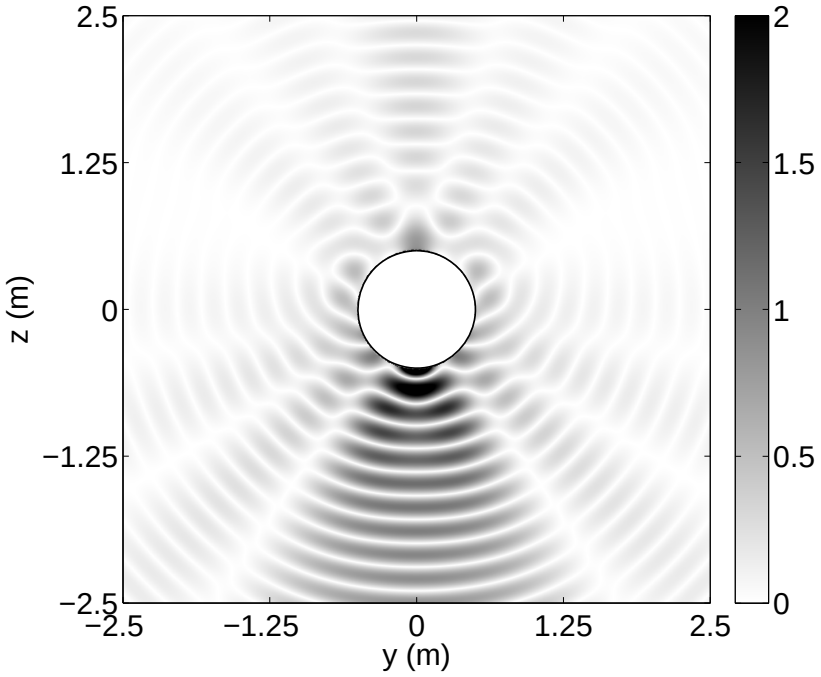
(c) 0.5 GHz, VV-Polarization

(d) 0.5 GHz, HH-Polarization

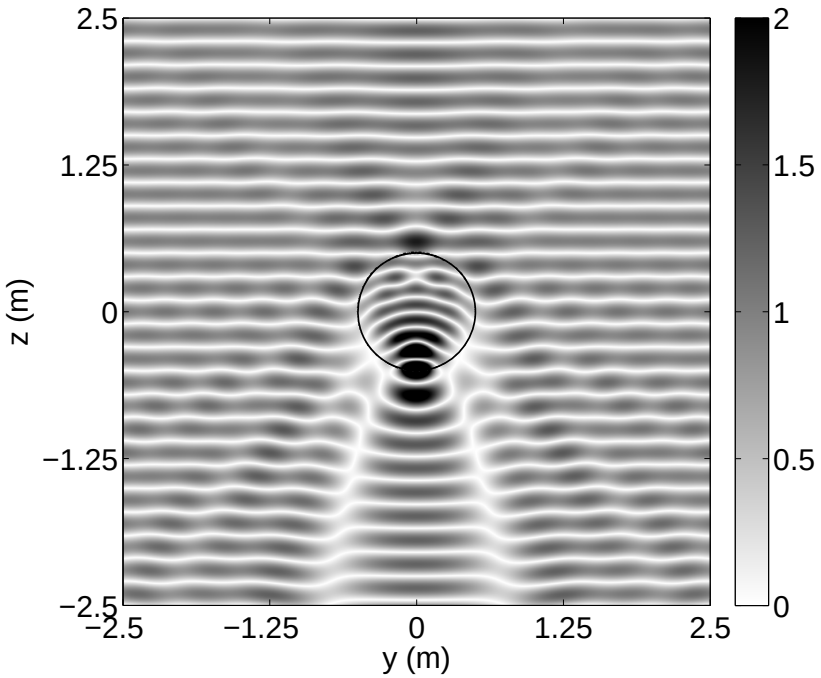
(e) 0.75 GHz, VV-Polarization

(f) 0.75 GHz, HH-Polarization

Figure 8.21: Lossy Dielectric Sphere ($\epsilon_r = 2.56 - j0.102$): Bistatic RCS



(a) Scattered Near Field ($|\mathrm{Re}(\mathbf{E}^s)|$, V/m)



(b) Total Near Field ($|\mathrm{Re}(\mathbf{E}^t)|$, V/m)

Figure 8.22: Dielectric Sphere: Near Field at 750 MHz

8.8.3.3 Coated Sphere

We next consider a conducting sphere with a thick dielectric coating. The radius of the conducting core is 0.25 meters, and is modeled using a mesh with 1280 near-equilateral triangles. The thickness of the dielectric coating is 0.25 meters, yielding an outermost radius of 0.5 meters. To describe the exterior surface, we again use the facet model from Section 8.8.3.1. This yields a total of 6400 triangles for both the inner and outer surfaces. The PMCHWT formulation is applied to the dielectric outer surface, and CFIE to the conducting core.

8.8.3.3.1 Monostatic RCS versus Frequency

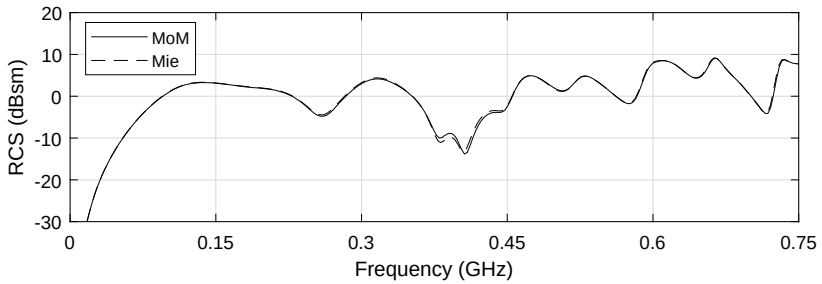
We first compute the RCS of the coated sphere for frequencies ranging from 10 to 750 MHz. In Figure 8.23a we compare the RCS obtained by the Mie series to the MoM in backscattering ($\theta^i = \theta^s = 0$) for a lossless coating ($\epsilon_r = 2.56$). The comparison is very good. In Figure 8.23b is a similar comparison for a lossy coating ($\epsilon_r = 2.56 - j0.102$). The forward-scattering RCS ($\theta^i = 0, \theta^s = \pi$) for each case is summarized in Figures 8.24a and 8.24b, respectively, where the agreement is again quite good.

8.8.3.3.2 Bistatic RCS

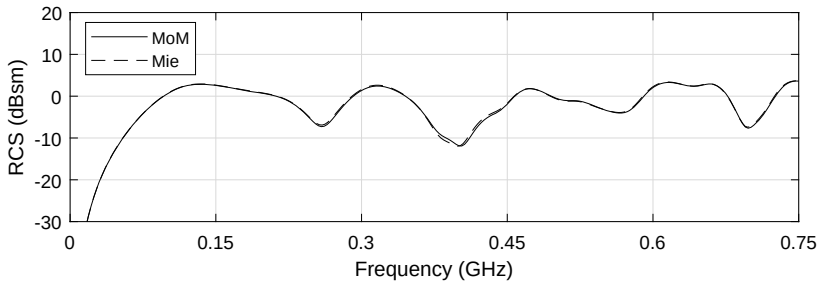
Using the same simulation parameters as before, we next consider the bistatic RCS at 0.25, 0.5, and 0.75 GHz. The MoM results are compared with the Mie series for the lossless coating in Figures 8.25a–8.25f. The comparison is very good. The results for the lossy coating are compared in Figures 8.26a–8.26f, where the comparison is again very good.

8.8.3.3.3 Near Field

Using (3.108) and (3.112), we compute the near field of the lossless coated sphere illuminated by an $\hat{\mathbf{x}}$-polarized plane wave incident from the $+\hat{\mathbf{z}}$ direction at 750 MHz. Figures 8.27a and 8.27b show the real part of the scattered and total electric field, respectively, in the yz plane. As with the dielectric sphere, the total near fields are computed separately in the external and internal dielectric regions, and are then overlaid.

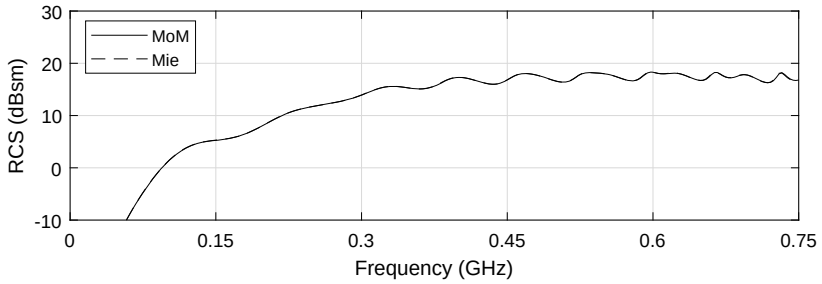


(a) Lossless Coated Sphere ($\epsilon_r = 2.56$)

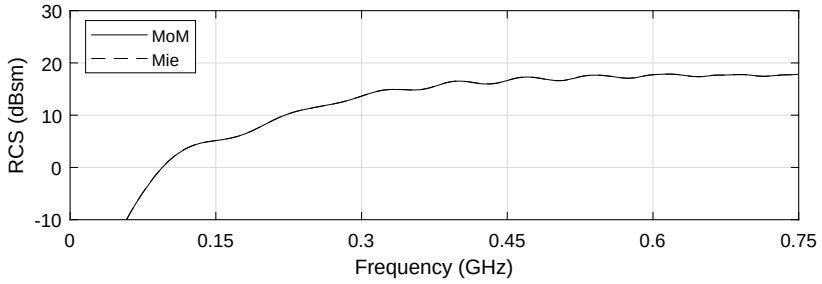


(b) Lossy Coated Sphere ($\epsilon_r = 2.56 - j0.102$)

Figure 8.23: Coated Sphere: Backscatter RCS vs. Frequency

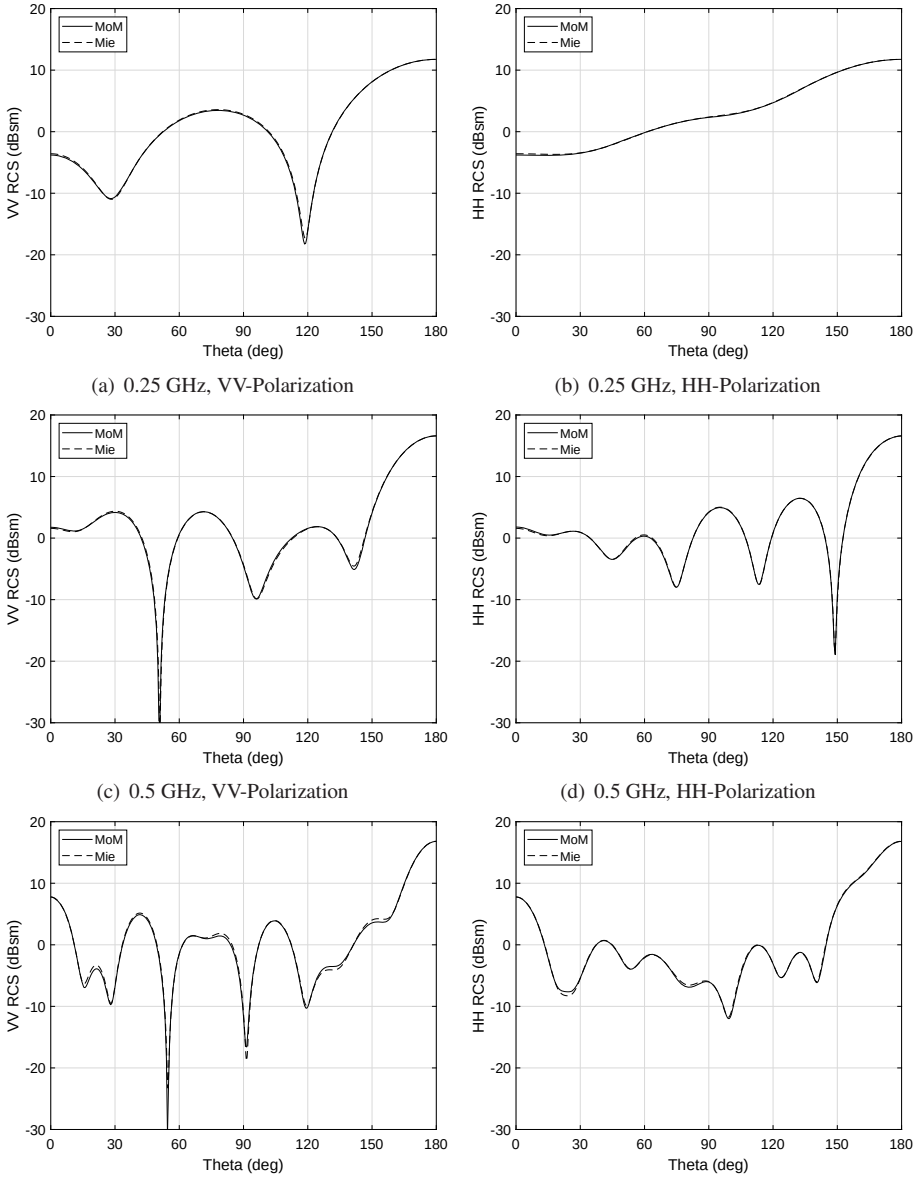


(a) Lossless Coated Sphere ($\epsilon_r = 2.56$)



(b) Lossy Coated Sphere ($\epsilon_r = 2.56 - j0.102$)

Figure 8.24: Coated Sphere: Forward Scatter RCS vs. Frequency



(a) 0.25 GHz, VV-Polarization

(b) 0.25 GHz, HH-Polarization

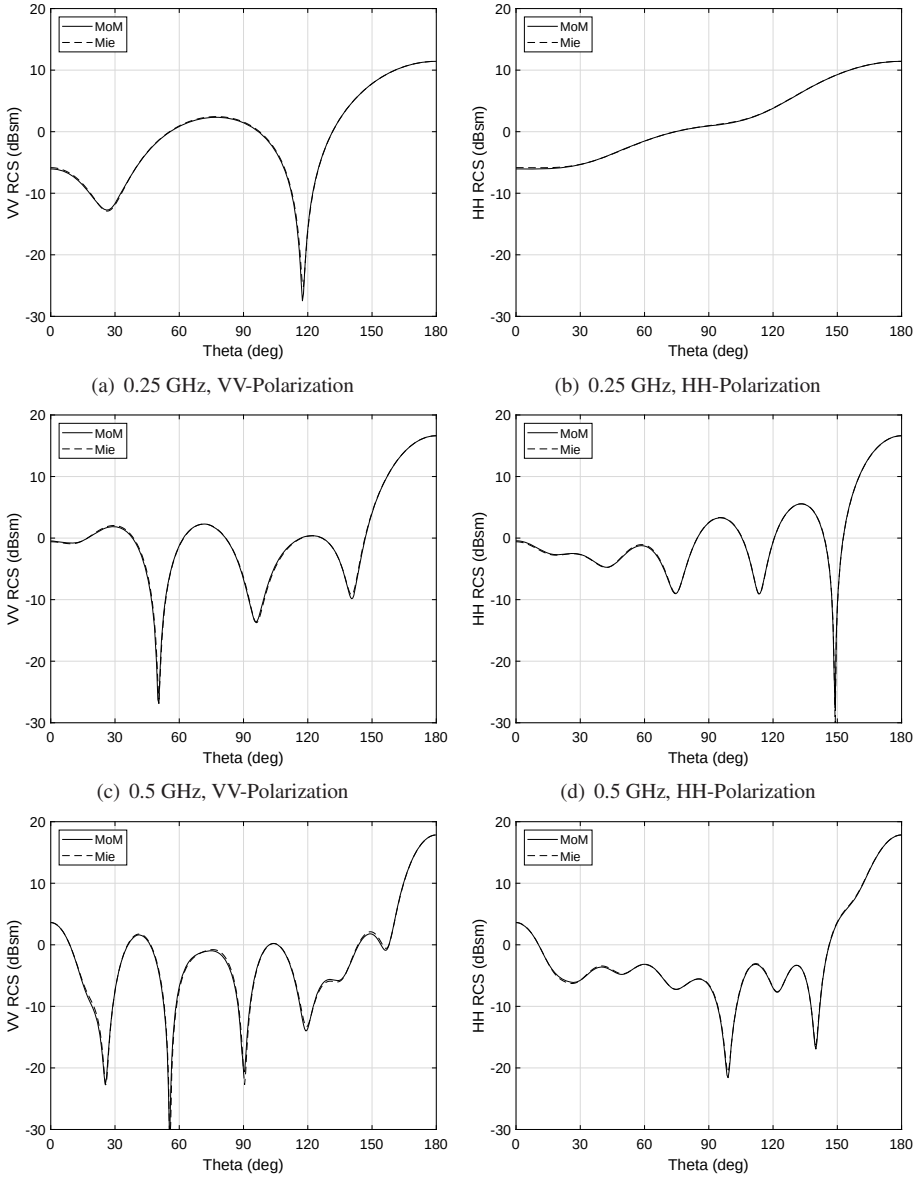
(c) 0.5 GHz, VV-Polarization

(d) 0.5 GHz, HH-Polarization

(e) 0.75 GHz, VV-Polarization

(f) 0.75 GHz, HH-Polarization

Figure 8.25: Lossless Coated Sphere ($\epsilon = 2.56$): Bistatic RCS



(a) 0.25 GHz, VV-Polarization

(b) 0.25 GHz, HH-Polarization

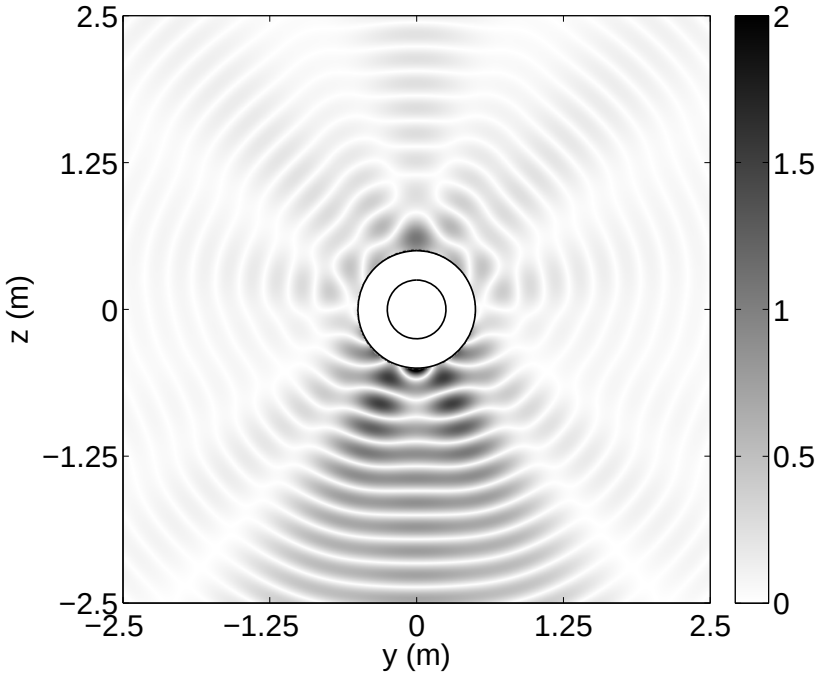
(c) 0.5 GHz, VV-Polarization

(d) 0.5 GHz, HH-Polarization

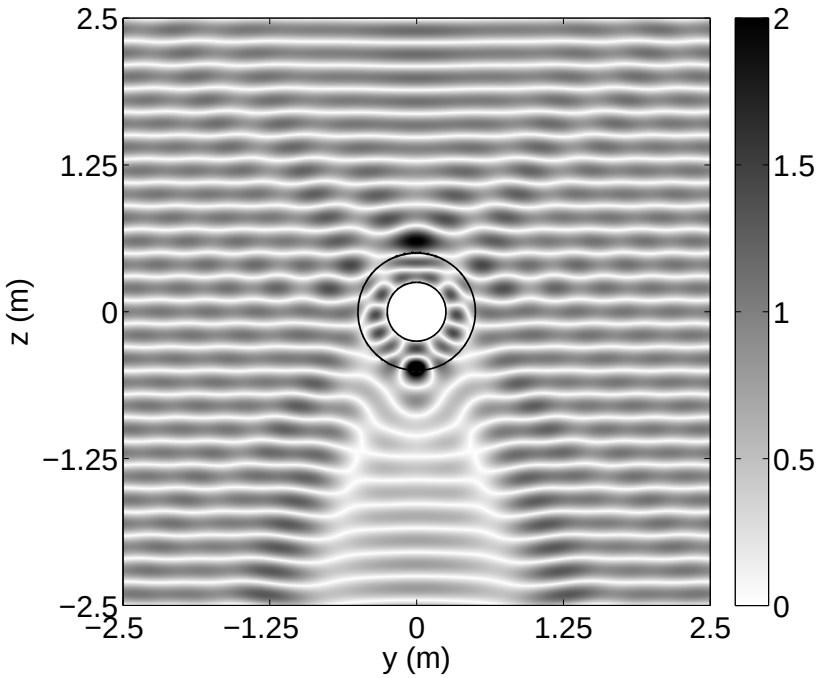
(e) 0.75 GHz, VV-Polarization

(f) 0.75 GHz, HH-Polarization

Figure 8.26: Lossy Coated Sphere ($\epsilon_r = 2.56 - j0.102$): Bistatic RCS



(a) Scattered Near Field ($|\mathrm{Re}(\mathbf{E}^s)|$, V/m)

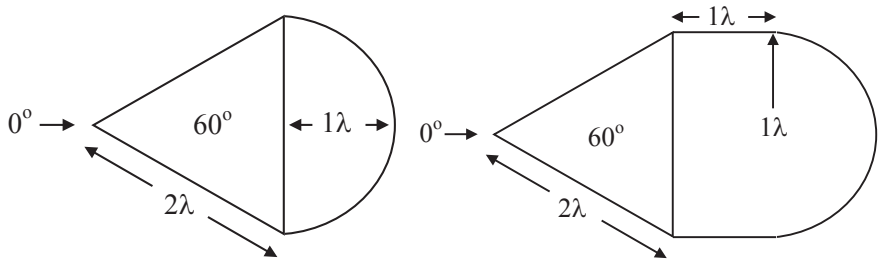


(b) Total Near Field ($|\mathrm{Re}(\mathbf{E}^t)|$, V/m)

Figure 8.27: Coated Sphere: Near Field at 750 MHz

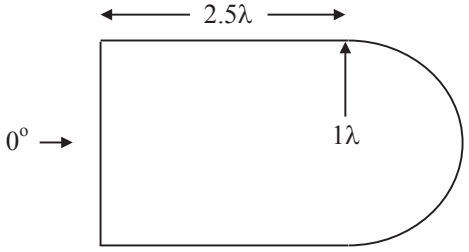
8.8.4 EMCC Plate Benchmark Targets

We next consider the EMCC benchmark plate radar targets that were described and measured in [22]. Because tip and edge diffractions were of primary interest in that paper, the measurements were performed using a conical cut 10 degrees from the plane of each target. The test articles were fabricated from aluminum foil or thin pieces of high-density foam coated with conducting paint. Thus, for each of our surface models we construct a thin sheet of planar facets, and for the MoM, the EFIE is used. In the plots that follow, the measurements were shifted in angle slightly to align them with the numerical results.

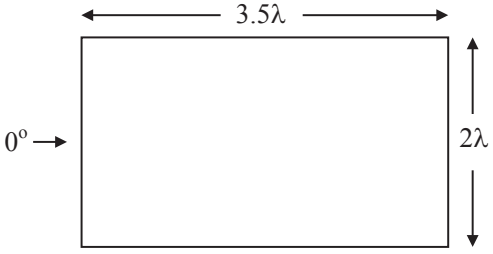


(a) Wedge Cylinder

(b) Wedge-Plate Cylinder



(c) Plate Cylinder



(d) Business Card

Figure 8.28: EMCC Plate Benchmark Targets

8.8.4.1 Wedge Cylinder

The wedge cylinder is shown in Figure 8.28a. The corresponding facet model, shown in Figure 8.29, comprises 3072 triangles. The monostatic RCS from the MoM is compared with the EMCC measurements in Figures 8.33a and 8.33b for vertical and horizontal polarizations, respectively. The comparisons are very good for both polarizations but are noticeably better in the horizontal case. In [22], the measurements were adjusted by 2 dB before plotting; however, that adjustment was not made here.

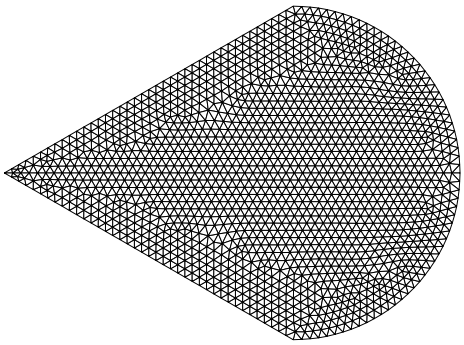


Figure 8.29: Facet Model of the Wedge Cylinder

8.8.4.2 Wedge-Plate Cylinder

The wedge-plate cylinder is shown in Figure 8.28b. The corresponding facet model, shown in Figure 8.30, comprises 4656 triangles. The monostatic RCS from the MoM is compared with the EMCC measurements in Figures 8.33c and 8.33d for vertical and horizontal polarizations, respectively. The comparisons are very good for both polarizations, although they are again slightly better in the horizontal case.

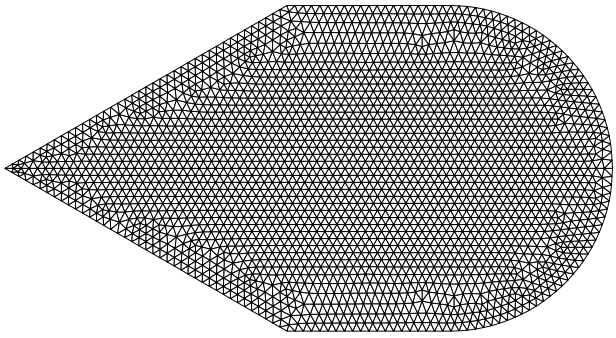


Figure 8.30: Facet Model of the Wedge-Plate Cylinder

8.8.4.3 Plate Cylinder

The plate cylinder is shown in Figure 8.28c. The corresponding facet model, shown in Figure 8.31, comprises 5058 triangles. The monostatic RCS from the MoM is compared with the EMCC measurements in Figures 8.33e and 8.33f for vertical and horizontal polarizations, respectively. The agreement is quite good, however the measurement has a higher amplitude than expected between $-45^\circ \leq \theta \leq 45^\circ$ and $100^\circ \leq \theta \leq 160^\circ$ in Figure 8.33e, the cause of which is unknown.

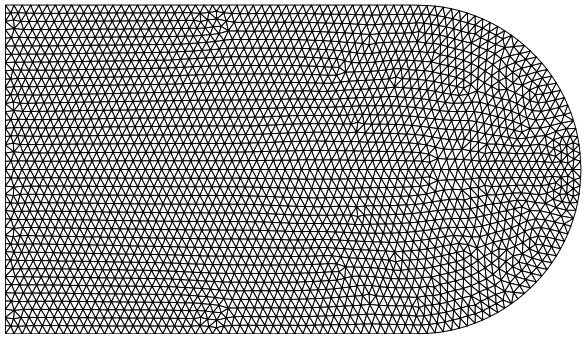


Figure 8.31: Facet Model of the Plate Cylinder

8.8.4.4 Business Card

The business card is shown in Figure 8.28d. The corresponding facet model, shown in Figure 8.32, comprises 5662 triangles. The monostatic RCS from the MoM is compared with the EMCC measurements in Figures 8.33g and 8.33h for vertical and horizontal polarizations, respectively. The comparison is very good for horizontal polarization, though the computed results are lower than the measurement for vertical polarization, which was also noted in [22].

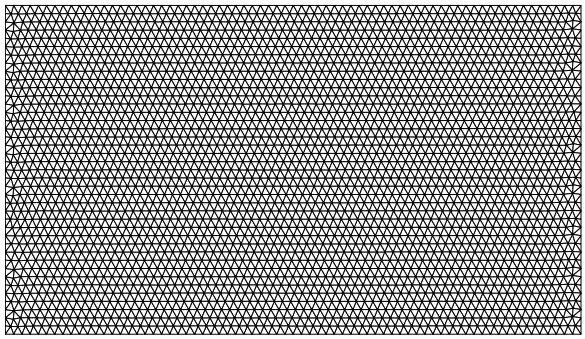
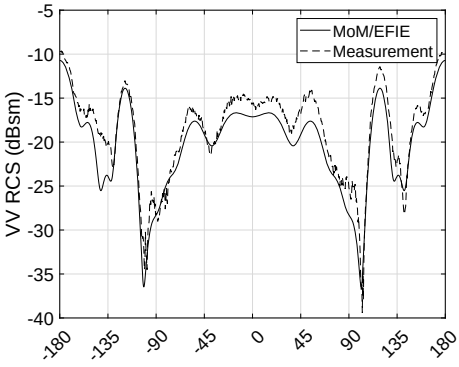
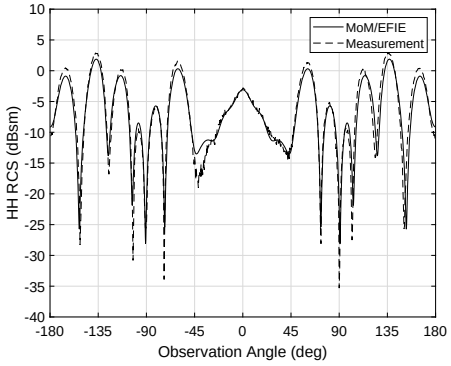


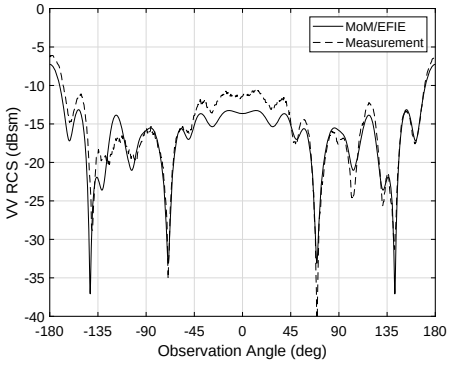
Figure 8.32: Facet Model of the Business Card



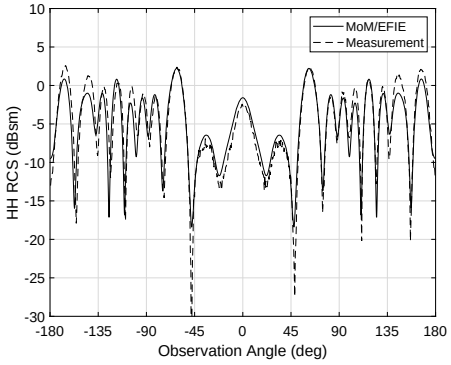
(a) Wedge Cylinder, VV-Polarization



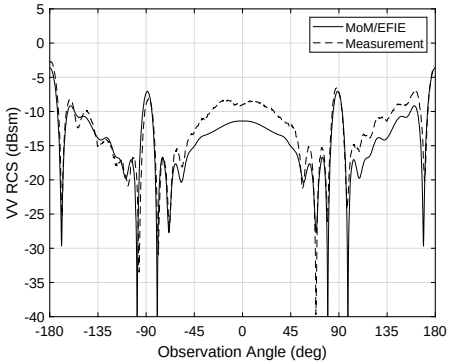
(b) Wedge Cylinder, HH-Polarization



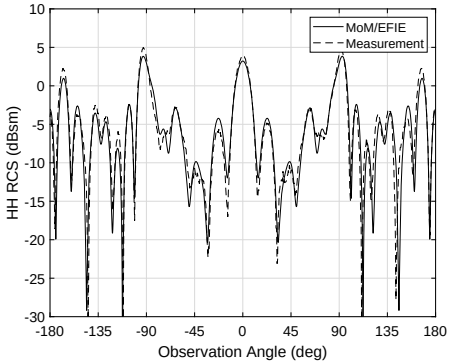
(c) Wedge-Plate Cylinder, VV-Polarization



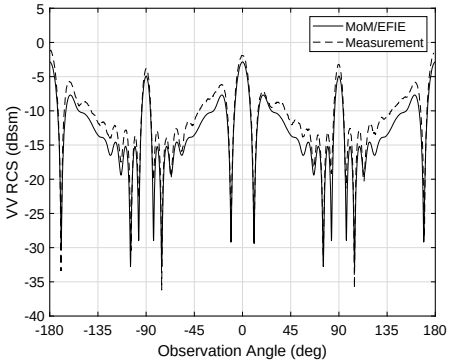
(d) Wedge-Plate Cylinder, HH-Polarization



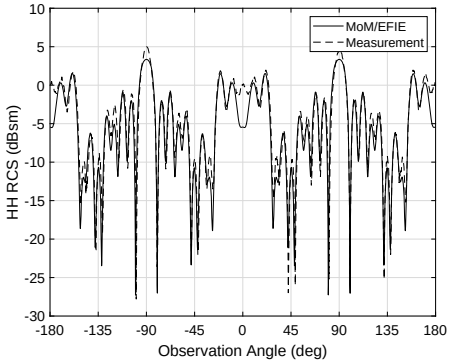
(e) Plate Cylinder, VV-Polarization



(f) Plate Cylinder, HH-Polarization



(g) Business Card, VV-Polarization



(h) Business Card, HH-Polarization

Figure 8.33: EMCC Plate Benchmark Targets: MoM vs. Measurement

8.8.5 Strip Dipole Antenna

We next consider the input impedance of a thin strip dipole antenna whose dimensions are outlined in Figure 8.34. This type of geometry is representative of thin foil chaff used as a radar countermeasure. The strip has length $L = 1$ m and width $w = 3$ mm, so Figure 8.34 is not to scale. The facet model comprises 400 triangles and is fed at the central edge (e_m) using the delta-gap model described in Section 8.3.3.2. Because the strip is very thin, the EFIE is used. The computed input resistance and reactance are shown in Figure 8.35 for frequencies between 10 MHz and 1 GHz. The first resonance is at approximately 150 MHz, where the dipole is $\lambda/2$ in length.

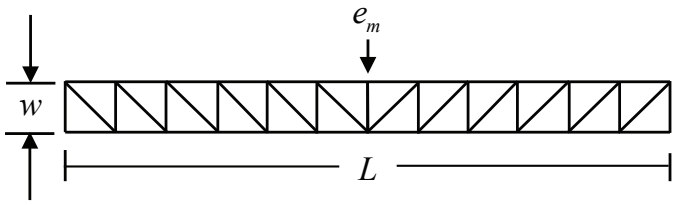


Figure 8.34: Strip Dipole Dimensions

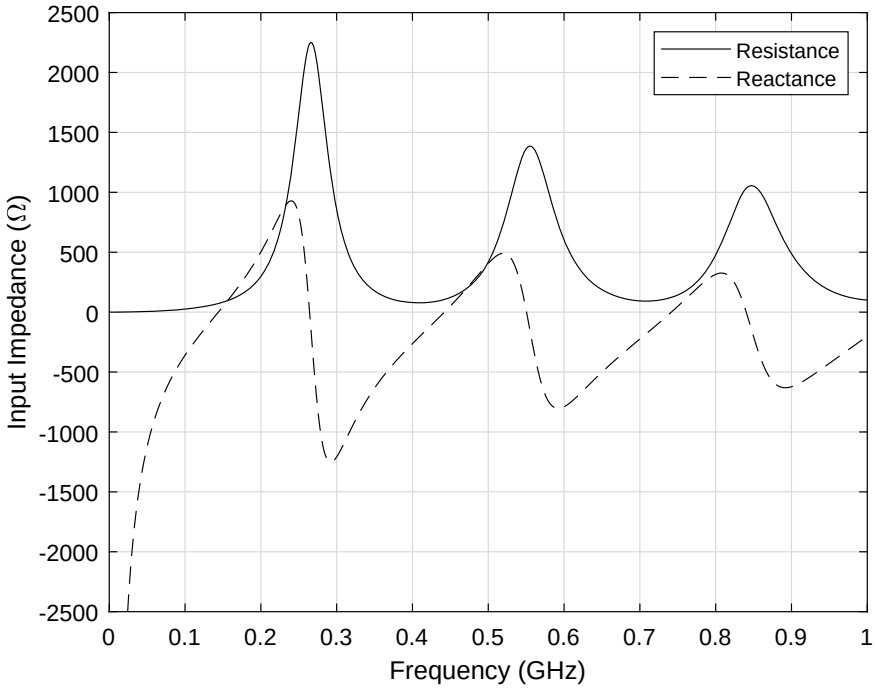


Figure 8.35: Strip Dipole Input Impedance

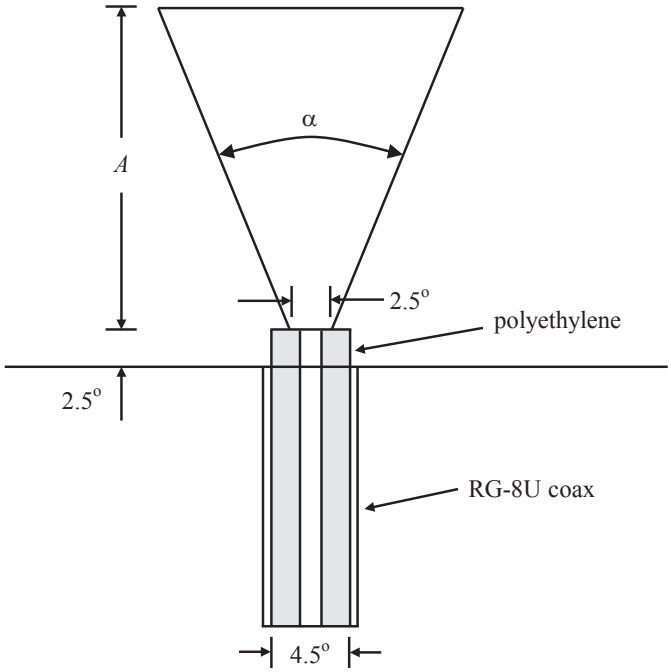
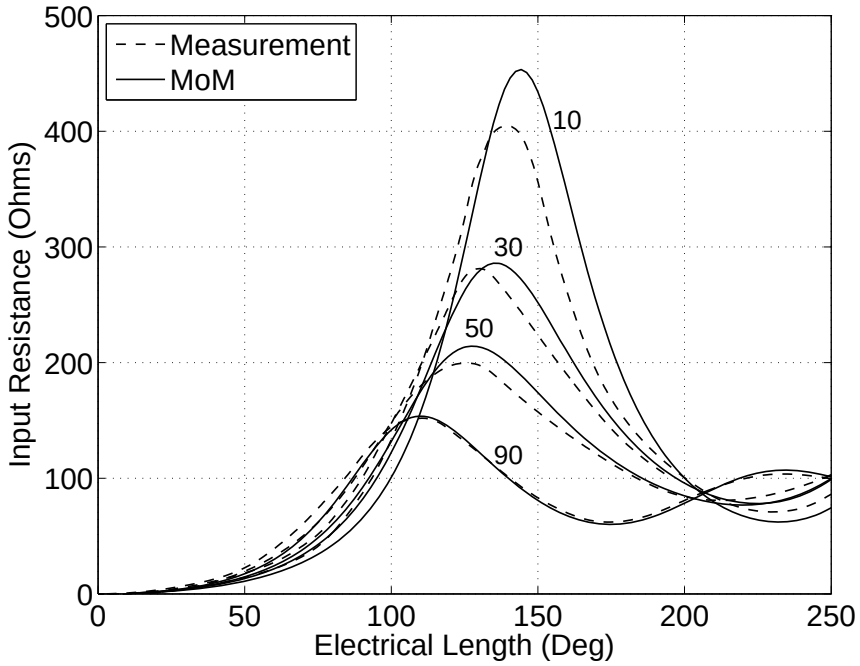


Figure 8.36: Bowtie Monopole Measurement Setup

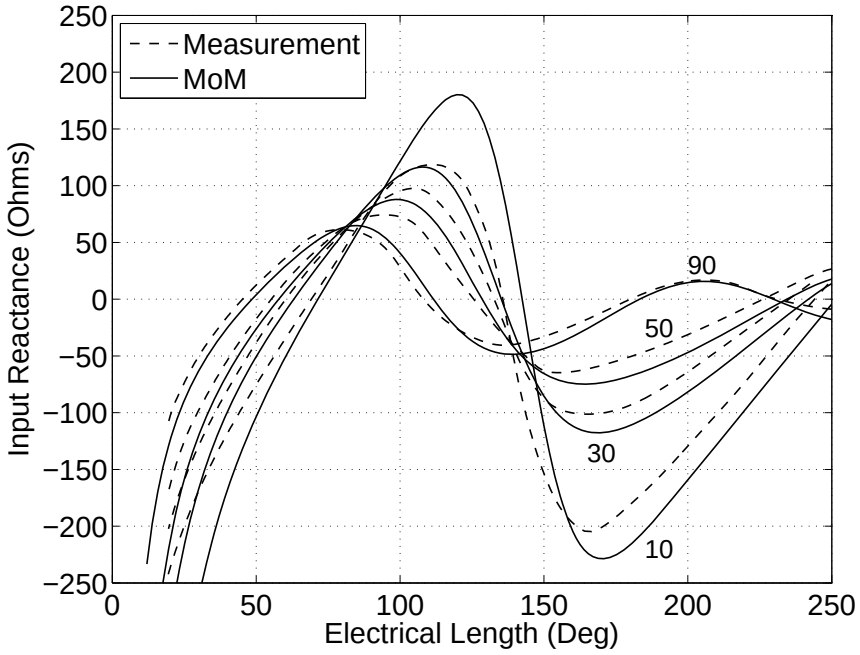
8.8.6 Bowtie Antenna

The planar bowtie antenna depicted in Figure 8.8a is used extensively in applications where a wide operating bandwidth is necessary. A study of the input impedance and radiation characteristics of the bowtie antenna was presented previously in [23] for various flare angles and lengths. Their measurement setup is illustrated in Figure 8.36, where a half-bowtie was fed and measured against a ground plane comprising a conducting disk 8 feet in diameter. The feed used an RG-8U coaxial cable that was trimmed and inserted through a hole in the disk. The fed end of the bowtie was truncated to facilitate an electrical connection to the center conductor of the cable. Measurements were obtained at a fixed frequency of 500 MHz using a slotted line with a sliding probe and transmission-line charts. Each antenna was fabricated to the maximum electrical length and physically cut down as the measurements were made. Therefore, the electrical dimensions of the feedpoint and ground plane remained constant.

For the MoM simulation, we model a full bowtie in free space and account for the fact that its input impedance will be approximately twice that of a half-bowtie over a finite conducting ground plane. Where the physical item was cut down to size at each step, in our case it makes more sense to fix the dimensions of the antenna and vary the frequency. We consider flare angles of 10, 30, 50, and 90 degrees, and the corresponding facet models comprise 826, 2010, 3462, and 7472 triangles, respectively. Each facet model has a half-length of 1 meter and an edge length of 2 cm at the feed-



(a) Resistance



(b) Reactance

Figure 8.37: Bowtie Input Impedance: EFIE vs. Measurement

point (see Figure 8.8a). In Figures 8.37a and 8.37b we compare the input resistance and reactance obtained from MoM with a delta-gap feed to the measurements in [23]. The agreement is fair, considering the differences between the physical and numerical models. The disparity between the delta-gap feed model and the physical setup is an obvious difference, and likely contributes to the observed offset between the resonant frequencies as well as the impedance amplitudes. A similar observation was made in [24]. If instead we had used the magnetic frill in Section 5.2.2 and reduced the physical length of the model rather than changing the frequency, the comparison might be better, though it would be more time-consuming in terms of setup and execution.

8.8.7 Archimedean Spiral Antenna

We next consider the characteristics of the Archimedean spiral antenna [25, 26], which has desirable broadband performance in terms of its input impedance as well as its circularly polarized radiation pattern. The geometry of this antenna is described in Figure 8.38a. The radius of each arm is linearly proportional to the angle and can be written as

$$r = b\phi + r_1 \tag{8.107}$$

and

$$r = b(\phi + \pi) + r_1 \ , \tag{8.108}$$

where r_1 is the starting radius and b is a constant that depends on the width w and spacing s of the arms of the antenna. If we choose a self-complementary spiral with $s = w$, then

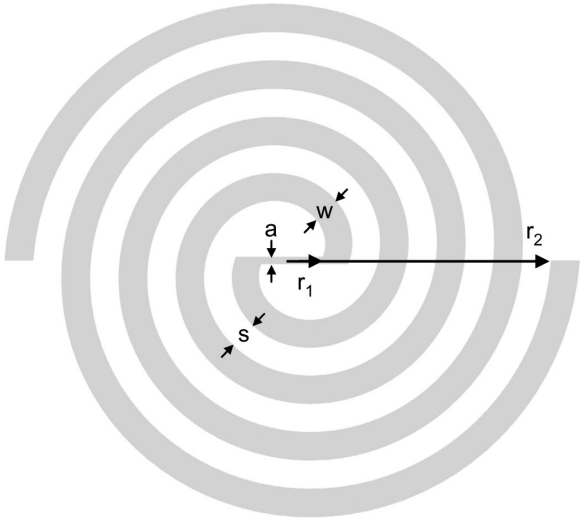
$$b = \frac{2w}{\pi} \ . \tag{8.109}$$

If the spiral has an infinite number of turns, then by Babinet's principle, the input impedance of the antenna should be approximately half that of the surrounding medium. If that medium is free space, then

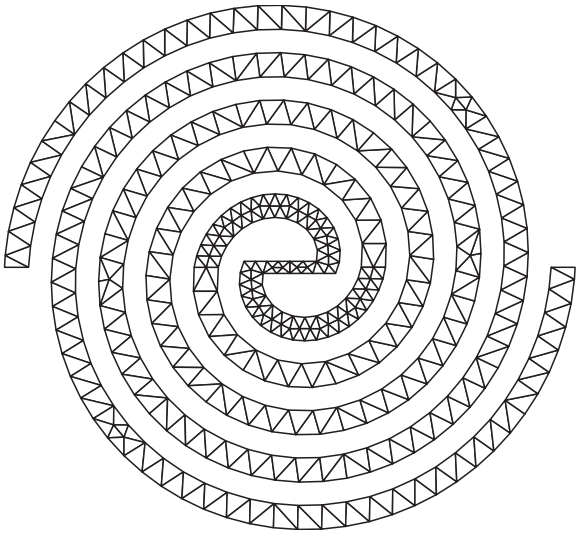
$$Z_{in} = \frac{\eta_0}{2} \approx 188.4\,\Omega \ . \tag{8.110}$$

When a voltage is applied to the center terminals of this antenna, it behaves in a manner similar to a two-wire transmission line and gradually transitions into a radiating structure where the circumference of the spiral is one wavelength [26]. In theory, an antenna with a larger number of turns should have broader bandwidth, however the available space limits its maximum size. A method of connecting the antenna to the feedline must also be devised. All of these considerations influence the final input impedance, which is not expected to agree exactly with the theoretical value of Z_{in}. For the numerical model, we choose a starting radius $r_1 = w$ and bridge the arms of the spiral at the center using a flat strip of width $a = w/2$. A heavier triangulation is used near the center, and a lower density is applied to the arms. This tessellation scheme is illustrated in Figure 8.38b, where the arms each comprise two and a half turns ($0 \le \phi \le \frac{5}{2}\pi$).

We now seek the dimensions of a spiral antenna having the flattest impedance characteristics between 1 and 5 GHz. To do so, we construct three spiral antennas, each with 8 turns per arm ($0 \le \phi \le 16\pi$), with widths w of 1, 2, and 4 mm. A delta-gap

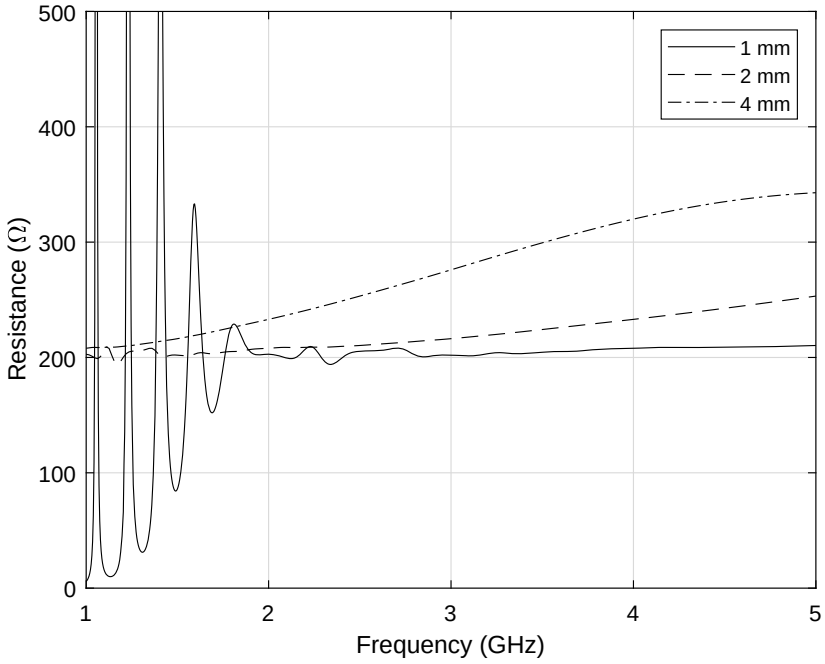


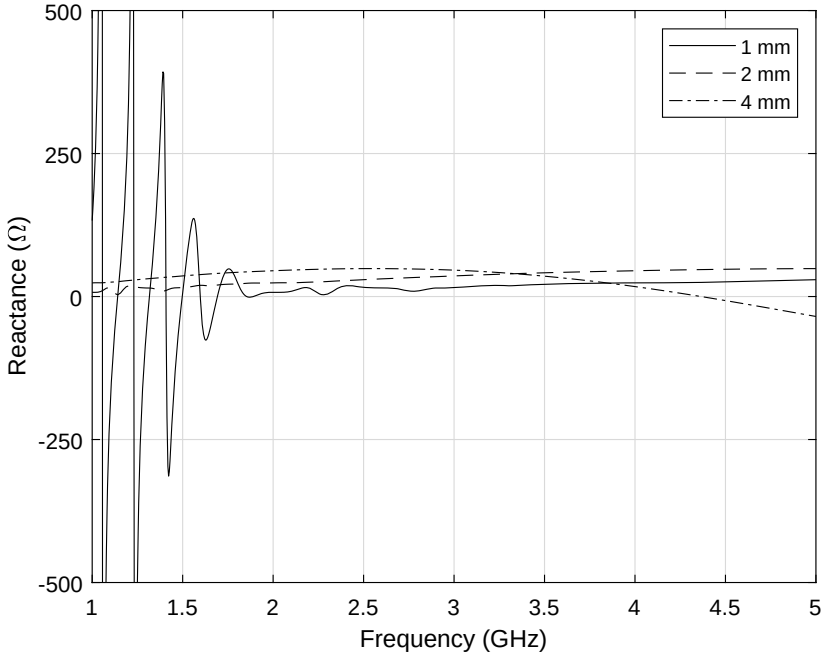
(a) Spiral Antenna Dimensions



(b) Example Spiral Antenna Mesh

Figure 8.38: Archimedean Spiral Antenna





(b) Reactance

Figure 8.39: Impedance of Spiral Antennas versus Frequency

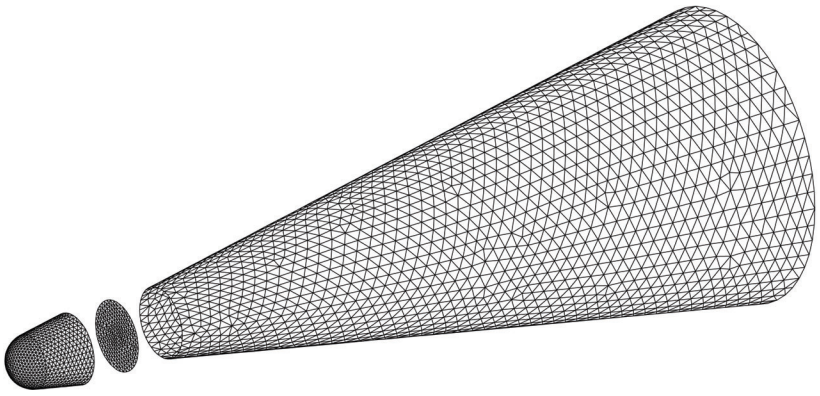


Figure 8.40: Monoconic RV with Dielectric Nose (Exploded View)

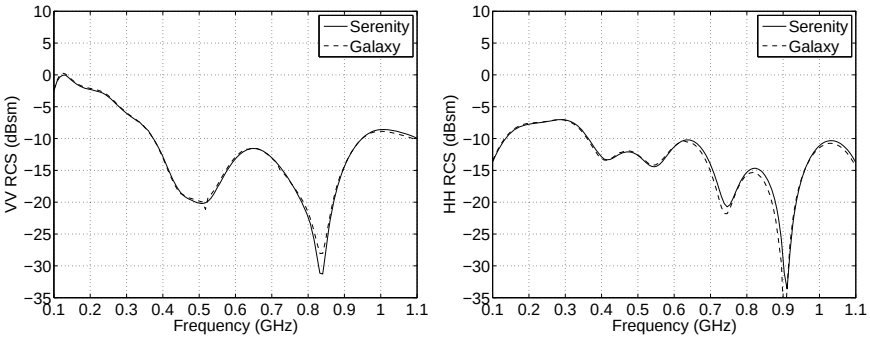
source is used to excite the edge at the center of the strip bridging the arms. The input resistance and reactance of each antenna are shown in Figures 8.39a and 8.39b, respectively. The 1 mm wide antenna has a nearly constant input resistance of approximately $210\,\Omega$ between 2 and 5 GHz and an input reactance of approximately $20\,\Omega$. The other two antennas vary more over this range, although their impedances are somewhat smoother at lower frequencies, which is expected given their larger overall dimensions. We expect that by adding more turns to the 1-mm antenna, its usable range could be extended down to 1 GHz with little impact on its higher-frequency performance. Using the 1-mm design as a starting point, a laboratory model could now be fabricated, and a more accurate estimate of the impedance could then be obtained by measuring it with a vector network analyzer (VNA).

8.8.8 Monoconic Reentry Vehicle with Dielectric Nose

Finally, we examine the monoconic reentry vehicle with dielectric nose, described previously in Section 7.10.2.4. The facet model of this object comprises three parts: the nose, septum, and frustum, which are modeled using 1944, 472, and 5824 triangles, respectively. These parts are shown in an exploded view in Figure 8.40. Because multiple bounces occur inside the dielectric nose, giving rise to more complex fields in that region, the mesh density on the nose and septum is higher than on the frustum. We consider two cases: a lossless nose ($\epsilon_r = 5$), and a lossy nose ($\epsilon_r = 5 - j0.25$).

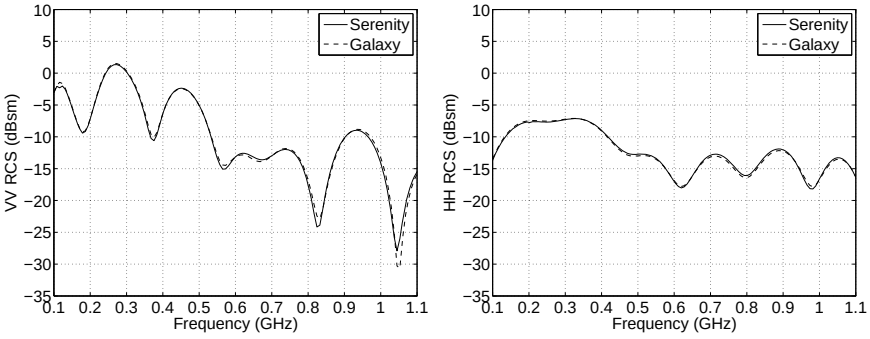
We first compare the monostatic RCS obtained by *Serenity* and *Galaxy* for frequencies ranging from 100 MHz to 1.1 GHz. The results for the lossless nose are compared at an incident angle of $\theta = \pi/4$ for vertical and horizontal polarizations in Figures 8.41a and 8.41b, respectively, where the comparison is fairly good. A similar comparison for the lossy nose is made at $\theta = 3\pi/4$ in Figures 8.42a and 8.42b, respectively, which is again fairly good.

We next compare the monostatic RCS for all angles at 1.1 GHz. The results for the lossless nose are compared for vertical and horizontal polarizations in Figures 8.43a and 8.43b, respectively. The comparison is fairly good. A similar comparison for the



(a) VV-Polarization (b) HH-Polarization

Figure 8.41: Monoconic RV with Lossless Nose: RCS vs. Frequency ($\theta = \pi/4$)



(a) VV-Polarization (b) HH-Polarization

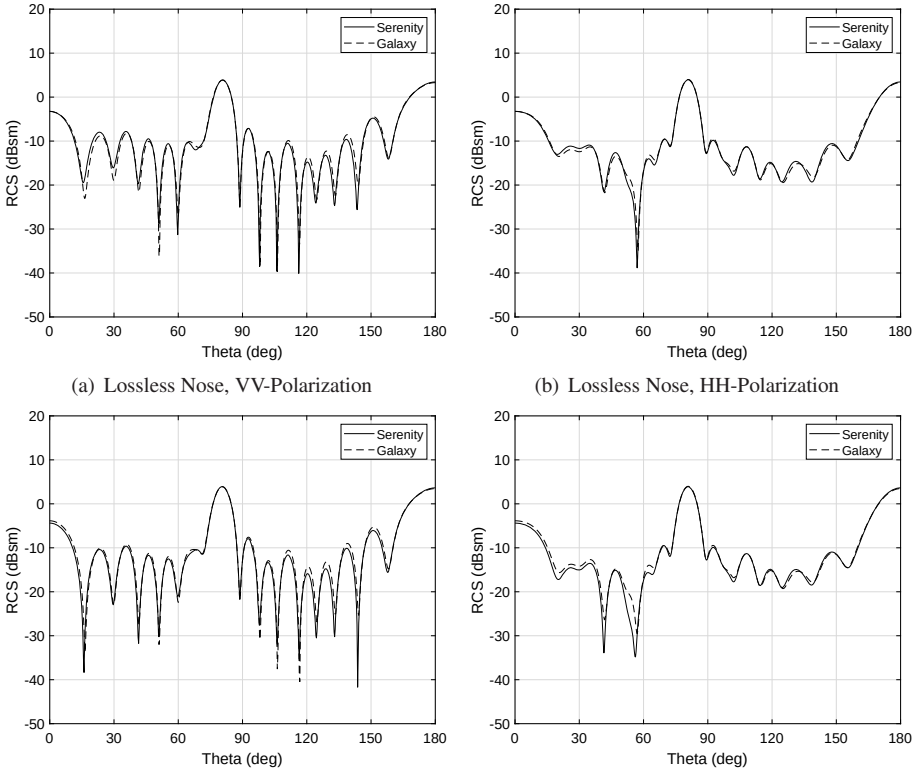
Figure 8.42: Monoconic RV with Lossy Nose: RCS vs. Frequency ($\theta = 3\pi/4$)

lossy nose is made in Figures 8.43c and 8.43d, respectively, where the comparison is fairly good. We observe that the lossy nose slightly reduces the RCS at forward-aspect angles, as expected.

8.8.9 Summary of Examples

Run metrics for the examples in this section are summarized in Table 8.5. Listed are the total number of electric and magnetic basis functions (N_J and N_M), and RAM ($M_{\mathbf{Z}}$, in MB) required to store the system matrix.

The Dell workstation used for these examples had 256 GB of RAM. Using 8 bytes for each single-precision complex value, a matrix with approximately 185,000 unknowns could be stored before all memory was exhausted. However, the actual limit is likely less, as it is unlikely that a single, contiguous array of that size would be available in RAM. In the following chapters, we demonstrate the solution of problems much larger than this limit on the same workstation using matrix compression techniques.



(a) Lossless Nose, VV-Polarization

(b) Lossless Nose, HH-Polarization

(c) Lossy Nose, VV-Polarization

(d) Lossy Nose, HH-Polarization

Figure 8.43: Monoconic RV RCS at 1.1 GHz

References

[1] P. Ylä-Oijala, M. Taskinen, and J. Sarvas, "Surface integral equation method for general composite metallic and dielectric structures with junctions," *Progress in Electromagnetics Research*, vol. 52, pp. 81–108, 2005.

[2] Rhinoceros 3D, Robert McNeel and Associates, rhino3d.com.

[3] L. Piegl and W. Tiller, *The NURBS Book*. Springer, 1995.

[4] J. Foley, A. van Dam, S. Feiner, and J. Hughes, *Computer Graphics: Principles and Practice*. Addison-Wesley, 1996.

[5] D. Wilton, S. Rao, A. Glisson, D. Schaubert, M. Al-Bundak, and C. M. Butler, "Potential integrals for uniform and linear source distributions on polygonal and polyhedral domains," *IEEE Trans. Antennas Propagat.*, vol. 32, pp. 276–281, March 1984.

Table 8.5: Run Metrics

Object	N_J	N_M	$M_{\mathbf{Z}}$
PEC Sphere (EFIE)	7680	0	450
PEC Sphere (nMFIE)	7680	0	450
PEC Sphere (CFIE)	7680	0	450
Dielectric Sphere	7680	7680	1800
Coated Sphere	9600	7680	2278
Wedge Cylinder	4537	0	157
Wedge-Plate Cylinder	6893	0	362
Plate Cylinder	7486	0	427
Business Card	8383	0	536
Strip Dipole	399	0	1.2
Bowtie (10°)	1151	0	10
Bowtie (30°)	2911	0	65
Bowtie (50°)	5067	0	196.9
Bowtie (90°)	11013	0	925
Spiral	4333	0	143
RV	12340	2896	1171

[6] S. Caorsi, D. Moreno, and F. Sidoti, "Theoretical and numerical treatment of surface integrals involving the free-space Green's function," *IEEE Trans. Antennas Propagat.*, vol. 41, pp. 1296–1301, September 1993.

[7] R. D. Graglia, "On the numerical integration of the linear shape functions times the 3-D Green's function or its gradient on a plane triangle," *IEEE Trans. Antennas Propagat.*, vol. 41, pp. 1448–1454, October 1993.

[8] T. F. Eibert and V. Hansen, "On the calculation of potential integrals for linear source distributions on triangular domains," *IEEE Trans. Antennas Propagat.*, vol. 43, pp. 1499–1502, December 1995.

[9] J. Jin, *The Finite Element Method in Electromagnetics*. John Wiley and Sons, 1993.

[10] S. Rao, D. Wilton, and A. Glisson, "Electromagnetic scattering by surfaces of arbitrary shape," *IEEE Trans. Antennas Propagat.*, vol. 30, pp. 409–418, May 1982.

[11] R. D. Graglia, D. R. Wilton, and A. F. Peterson, "Higher order interpolatory vector bases for computational electromagnetics," *IEEE Trans. Antennas Propagat.*, vol. 45, pp. 329–342, March 1997.

[12] D. Sievers, T. F. Eibert, and V. Hansen, "Correction to 'on the calculation of potential integrals for linear source distributions on triangular domains'," *IEEE Trans. Antennas Propagat.*, vol. 53, p. 3113, September 2005.

[13] M. G. Duffy, "Quadrature over a pyramid or cube of integrands with a singularity at a vertex," *SIAM J. Numer. Anal*, vol. 19, pp. 1260–1262, December 1982.

[14] A. Tzoulis and T. Eibert, "Review of singular potential integrals for method of moments solutions of surface integral equations," *Advances in Radio Science*, vol. 2, pp. 97–99, 2004.

[15] W. C. Chew, J. M. Jin, E. Michielssen, and J. Song, *Fast and Efficient Algorithms in Computational Electromagnetics*. Artech House, 2001.

[16] P. Ylä-Oijala and M. Taskinen, "Calculation of CFIE impedance matrix elements with RWG and n x RWG functions," *IEEE Trans. Antennas Propagat.*, vol. 51, pp. 1837–1846, August 2003.

[17] R. E. Hodges and Y. Rahmat-Samii, "The evaluation of MFIE integrals with the use of vector triangle basis functions," *Microw. Opt. Tech. Lett.*, vol. 14, pp. 9–14, January 1997.

[18] L. S. Blackford, J. Choi, A. Cleary, E. D'Azevedo, J. Demmel, I. Dhillon, J. Dongarra, S. Hammarling, G. Henry, A. Petitet, K. Stanley, D. Walker, and R. C. Whaley, *ScaLAPACK Users' Guide*. Philadelphia, PA: Society for Industrial and Applied Mathematics, 1997.

[19] K. Faison, "The Electromagnetics Code Consortium," *IEEE Antennas Propagat. Magazine*, vol. 30, pp. 19–23, February 1990.

[20] J. S. Zhao and W. C. Chew, "Integral equation solution of Maxwell's equations from zero frequency to microwave frequencies," *IEEE Trans. Antennas Propagat.*, vol. 48, pp. 1635–1645, October 2000.

[21] J. F. Lee, R. Lee, and R. J. Burkholder, "Loop star basis functions and a robust preconditioner for EFIE scattering problems," *IEEE Trans. Antennas Propagat.*, vol. 51, pp. 1855–1863, August 2003.

[22] A. C. Woo, H. T. G. Wang, M. J. Schuh, and M. L. Sanders, "Benchmark plate radar targets for the validation of computational electromagnetics programs," *IEEE Antennas Propagat. Magazine*, vol. 34, pp. 52–56, December 1992.

[23] G. H. Brown and J. O. M. Woodward, "Experimentally determined radiation characteristics of conical and triangular antennas," *RCA Review*, pp. 425–452, 1952.

[24] C. Leat, N. Shuley, and G. Stickley, "Triangular-patch model of bowtie antennas: Validation against Brown and Woodward," *IEE Proc.-Microw. Antennas Propag.*, vol. 145, pp. 465–470, December 1998.

[25] W. L. Curtis, "Spiral antennas," *IRE Trans. Antennas Propagat.*, vol. 8, pp. 298–306, May 1960.

[26] J. A. Kaiser, "The Archimedean two-wire spiral antenna," *IRE Trans. Antennas Propagat.*, vol. 8, pp. 312–323, May 1960.